Future Batteries 10 (2026) 100181

Contents lists available at ScienceDirect

Future Batteries

journal homepage: www.sciencedirect.com/journal/future-batteries

Simulative determination of the composition-dependent effective thermophysical parameters of established and future battery electrodes

Raphael Mühlpfort *, Leonie Pfeifer, Thomas Wetzel, Philipp Seegert

Karlsruhe Institute of Technology (KIT), Institute of Thermal Process Engineering (TVT), Heat and Mass Transfer, Kaiserstr. 12, Karlsruhe 76131, Germany

ARTICLE INFO

Keywords:
Lithium-ion battery
Sodium-ion battery
Thermal conductivity
Heat capacity
Density

ABSTRACT

Thermal management is essential for the performance, lifetime and safety of intercalation batteries like lithium-ion batteries (LIB), especially in large cell assemblies used in electric vehicles or stationary storage systems. With the emergence of ever newer cell technologies such as next-generation LIB or sodium-ion battery materials, the design of thermal management systems is constantly facing new challenges, as these new cell generations are usually not sufficiently characterized. The huge variety of materials and designs at the electrode level influences the thermal behavior of the entire cell. The aim of this work is to derive the effective thermal transport parameters for different electrode configurations by means of modeling, based on the thermophysical variables of the individual components and the composition. By specifically varying the input parameters, a spectrum of the possible thermal properties is demonstrated and a corresponding database provided. The focus of the thermophysical data is on thermal conductivity, density, and specific heat capacity for commercial and future technically relevant lithium and sodium-ion battery (SIB) systems.

Introduction

Intercalation batteries have become the preferred energy storage system in electric vehicles (EVs) [1]. Especially lithium-ion batteries (LIBs) have excelled in the recent years due to their high volumetric and gravimetric energy density, low self-discharge rate and high cycle stability compared to other electrochemical energy storage systems [2]. To increase the energy density, improve the lifetime and the stability of battery cells, particularly in the case of fast charging and discharging rates, and also to reduce the costs of the battery pack, the most expensive part of an EV [3], the components and the design of the cells are continuously being developed further.

Next to the electrical and mechanical properties, the thermophysical properties are also of essential importance for the commercial use of batteries. The temperature level and distribution of a battery cell in an EV is influenced, on the one hand, by the heat release caused by loss processes and reactions inside the cell during operation. On the other hand, they are also influenced by the heat transfer with the thermal management system and the environment. The effective thermal conductivity, density and specific heat capacity are the central parameters that determine the transient thermal behavior of a battery. These effective thermal transport parameters, based on the materials used and the microstructure of the electrodes, influence the behavior from the single cell to the entire cell pack. These parameters are therefore of central importance for the design of an efficient thermal management system in the vehicle to ensure maximum performance, a long lifetime and safety in operation. Through a well-founded thermal conditioning of the cells, degradation effects can be minimized and an enhanced performance can be achieved [4].

One aspect of the further development of batteries is to increase the proportion of active material (AM) and to reduce the share of inactive components of the electrode coating such as binder (B) and conductive additive (CA). The production of functional battery electrodes with a sufficiently contacted binder-conductive-additive-network requires a good understanding of the cell manufacturing process. Further developing the active material is another way to improve the cell in performance and costs. At the electrode level, a wide variety of designs is possible due to the combination of materials used and the microstructural properties resulting from the manufacturing process, which decisively define the effective transport parameters of the porous electrode microstructure.

Fig. 1, which schematically shows the complex inner structure of the electrochemical basic unit of an intercalation battery like a LIB or SIB, is intended to illustrate the options for variations in material and

* Corresponding author.
E-mail address: raphael.muehlpfort@kit.edu (R. Mühlpfort).

https://doi.org/10.1016/j.fub.2026.100181
Received 18 March 2026; Received in revised form 27 April 2026; Accepted 29 April 2026
Available online 4 May 2026

composition. Based on the design of commercially established LIB systems to date, there are several customization options for future lithium-ion and sodium-ion batteries. For newer generations of lithium-ion cells, the use of graphite-silicon blends or elemental lithium as anode active material should be mentioned in addition to novel cathode intercalation materials like nickel-rich NMC [5]. The change of the intercalation ion from lithium to sodium also requires an adaption of the active materials used. Analogous to LIBs with graphite, hard carbon has emerged as preferred anode material for SIBs [6], while on the cathode side there is a wide variety of materials with potential relevance for technical applications. The similar operating and manufacturing principles of LIBs and SIBs enables a good transfer of knowledge between the two systems, and SIBs offer the potential for a more cost-effective option and drop-in technology for the future [7].

The overall thermal behavior of battery cells and packs is determined at the material level by the selection, composition ratio, and underlying microstructure of the electrodes. The pairing of the electrodes, the selection of the separator and electrolyte, and the corresponding cell format also determine differences in the heat transfer paths from the cell and pack to the environment. This huge variety of parameters influencing the effective thermophysical properties of the battery cell requires appropriate characterization for each application, especially in mobile systems where weight and space are limited. The use of simulations has proven to be a useful tool for accelerating the design of cell system assemblies while minimizing costly and time-consuming characterizations. As shown in Fig. 1, the smallest common unit for different cell formats is the electrode level, where the effective properties of the coating are subject to particularly high variance.

In the literature some data on thermophysical properties of established LIB can be found on electrode or cell level based on different determination methods, for example in Steinhardt et al. [8], or Spitthoff et al. [9]. but the literature does not provide a comprehensive description, as the exact electrode composition or material combination is often unknown. The sparse data basis of the effective thermal transport parameters depending on the composition, especially for newer cell chemistries, makes it difficult to apply literature data in simulation tools for system designs and transfer to practical applications. The objective of this work is to determine the effective thermophysical values of the thermal conductivity, density, and specific heat capacity of the electrode as a function of composition, based on the pure substance properties of the materials. This paper presents comprehensive research on the thermophysical pure substance data of established and possible future technically relevant active materials. This data is then used to calculate the effective values for thermal conductivity, density, and specific heat capacity of the electrodes with a variation in pure substance properties and composition. In addition to the absolute values, the results also provide information about the influence depending on the variation variables and, consequently, about their sensitivity influence, thus creating a basis for evaluation. The effective values for density and specific heat capacity are calculated on a proportion basis, while thermal conductivity is calculated using an analytical model approach. For selected cases, heterogeneous electrode structures are replicated with a 3D microstructure model and the values of the analytical model are checked and critically evaluated. Overall, the thermal properties of different electrode configurations are determined for different active materials and the results obtained are plotted in scatter diagrams.

Composition of battery electrodes and thermophysical parameters of individual materials

The effective thermal conductivity, density and specific heat capacity are determined based in the pure substance properties of the individual materials and are determined for the respective electrodes. The active materials considered in this work are listed in Table 1 and are categorized into lithium- and sodium-based active materials as well as cathode and anode systems. The selection was made based on technically established battery materials offered by commercial material and electrode manufacturers like NEI Corporation [10] and MTI Corporation [11]. In the following calculation and simulative determination of the effective thermophysical properties (Section 3), only the active material is varied and binder, conductive additive and electrolyte from established LIB-systems are used as a reference base to enable a better comparison of the electrode systems with each other.

Further, to improve comparability between the individual systems, standardized weight fractions w^s are to be defined for the respective electrode components of active material w^s_{AM}, conductive additive w^s_{CA} and binder w^s_B. The weight fractions of the solid components based on the solid phase are listed in Table 2 for anode and cathode systems and

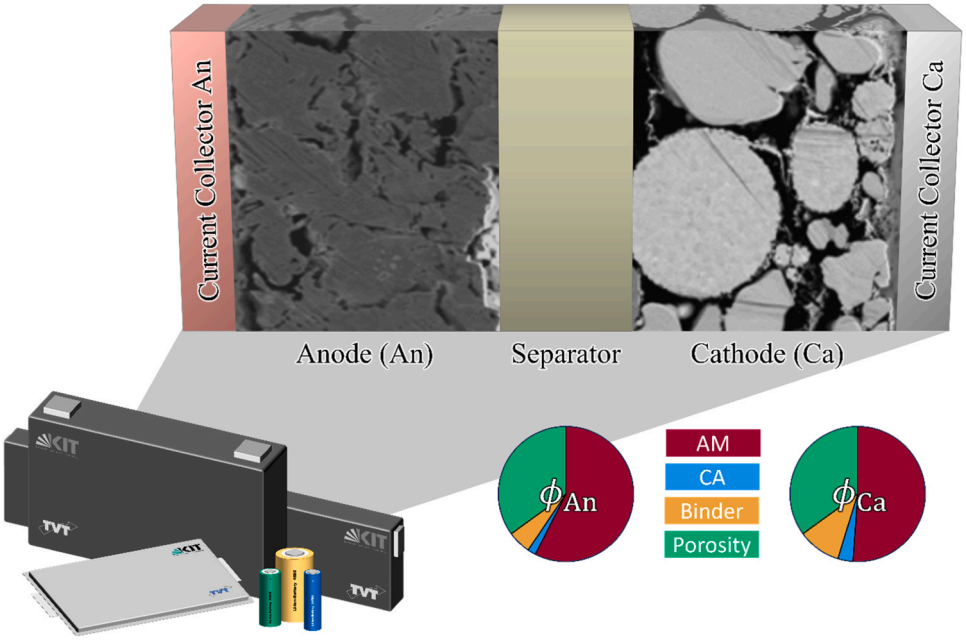

Fig. 1. Schematic representation of the internal structure of the electrochemical basic unit of an intercalation battery and the variation options of the chosen materials.

Table 1
Overview of the investigates materials subdivided into Li- and Na-based active materials and electrode additive materials, cathode and anodes systems.

Component	Li-based active material		Na-based active material	
Cathode	LCO	$LiCoO_2$	NFM	$NaNi_xFe_yMn_zO_2$
	LFP	$LiFePO_4$	NFP	$NaFePO_4$
	LMFP	$LiMn_xFe_{1-x}PO_4$	NMO	Na_xMnO_2
	LMNO	$LiMn_{1.5}Ni_{0.5}O_4$	Pr. Blue	$Na_2Fe_2(CN)_6$
	LMO	$LiMn_2O_4$	Pr. White	$Na_2Mn[Fe(CN)_6]$
	NCA	$LiNi_xCo_yAl_zO_2$	NCP	$NaCoPO_4$
	NMC	$LiNi_xMn_yCo_zO_2$	NMP	$NaMnPO_4$
	V2O5	LiV_2O_5	NNMO	$Na_xNi_yMn_{1-y}O_2$
			NNP	$NaNiPO_4$
			NVP	$Na_3V_2(PO_4)_3$
Anode	Li	Lithium	Na	Sodium
	C_6	Graphite	NVO	$NaVO_3$
	Si	Silicon	HC	Hard Carbon
	LTO	$Li_4Ti_5O_{12}$	NTO	$Na_xTi_yO_z$
	TNO	$TiNb_2O_7$	NTP	$NaTi_2(PO_4)_3$

are each divided into three configurations. The base configuration represents an average electrode composition as found in real systems. A comparison of different electrode compositions from commercial suppliers can be found in supplementary section S3. Based on this, so called upper and lower configurations are also be considered. The data for the upper configuration refer to established electrode systems in which the proportion of binder and conductive additive can be minimized because a functional electrode can be produced with knowledge of the processability. In contrast, the lower configuration requires a higher binder and conductive additive content in order to form a sufficiently good binder-conductive additive (BCA) network. In order to ensure sufficient electrical contact between the active material particles, the total mass fraction of conductive additive in the solid phase was kept almost identical and only the binder fraction of the total electrode was reduced. This results in an increasing proportion of conductive additives in the entire binder-conductive additive phase. In addition to the solid composition, porosities ϵ were also defined for the respective configurations.

The conversion of the mass fractions w_i with Eq. (1) and the corresponding densities ρ_i leads to the volume fractions ϕ_i^s of the solid phase of the electrode. In addition to the proportions for the solid phase, the porosity ϵ for the respective configuration is specified. The proportions of the solid components within the entire electrode ϕ_i^{El} are converted from their respective proportions in reference to the solid phase using Eq. (2).

$$\phi_i^s = \frac{w_i^s / \rho_i}{\sum_j^n w_j^s / \rho_j} \tag{1}$$

$$\phi_i^{El} = \frac{(100 \quad Vol\% - \epsilon) \cdot \phi_i^s}{100} \tag{2}$$

To calculate the effective values of the electrodes, the pure substance values for thermal conductivity, density and specific heat capacity of the individual materials are required in addition to the mass fractions. In an extensive literature research, pure substance data for the thermophysical material properties were compiled from the literature, material databases, and manufacturer specifications. Since no definite statement can be made about the state of charge, temperature dependency or different crystal structures due to the limited data available in the literature, fluctuation ranges are defined for the individual materials to take possible uncertainties and variations in our following calculations into account. Publications such as those by Marconnet et al. [12], Pfeifer et al. [13], Oehler et al. [14], and Steinhardt et al. [8]. demonstrate the influence of temperature and state of charge or degree of intercalation on the thermophysical properties of battery electrodes and on the overall cell. However, this dependence is influenced by a large number of electrode and microstructure parameters and is particularly poorly understood for newer materials such as those used in SIBs. Since no clear database is available, the variation ranges for the thermophysical properties were selected generically in this work based on the compiled data to demonstrate the influence of fluctuations of pure substance data on the electrode level. The data compiled from the literature [14–150] on thermal conductivity, density, and specific heat capacity are summarized in Fig. 2 and are also listed separately, with references to the corresponding sources, in the supplementary information S2.

The defined variation ranges of the thermal conductivity, density and specific heat capacity for subsequent study in Section 3, consisting of a base configuration and a lower and upper limit are summarized in Table S4a and S4b. In addition to the literature values (Index: L) also the selected base configuration (Index: B) with the defined fluctuation range (Index: Range Min/Max) are shown in Fig. 2. Table S4b provides an overview of the electrochemically interactive components. Variation ranges are also specified for the solid components of the coating, while the pore medium is assumed to be constant.

In addition, a calculation according to the approach by Kopp [151] was used for determining the specific heat capacity of the pure substances of battery materials. This approach is based on the structural formular-weighted proportions of the elements N_i and the similarity of the specific molar heat capacities $\widetilde{c}_{p,i}$. With the help of the molar masses $\widetilde{M}_i$, this substance-related approach can be converted into mass-related quantities using Eq. (3). The supplementary section S1 summarizes the molar masses and specific molar heat capacities according to Kopp for the known elements. For elements without a value according to Kopp, the default value designated as “Misc” should be used [151]. With knowledge of the structural formula, the specific heat capacities according to Kopp can be calculated for the active materials. Furthermore, it should be noted that this approach doesn’t take into account any dependency on the state of charge or the temperature and the values apply to a temperature of about 298 K. When comparing the literature values in Fig. 2 with the values calculated using the approach by Kopp, the results provide a good estimate for the materials shown here, as can be seen in the examples of graphite, LCO, NMC, and LFP. Nevertheless, it should be noted that materials such as LMO, LTO, or NVO are underestimated by up to 20 % relative to the defined base value. The Kopp calculation provides a good estimate, but it does not allow for universal applicability nor does it serve as a sufficient substitute for experimental characterization as already shown by studies of Kriegel et al. [152] and Zienert et al. [153].

Table 2
Mass fractions of the solid components’ active material, conductive additive and binder, based on the solid phase of the electrode coating, the ratio of conductive additive in the BCA-phase and the volumetric porosity.

	Cathode			Anode		
	lower configuration	base configuration	upper configuration	lower configuration	base configuration	upper configuration
w^s_{AM} / Ma%	85	90	95	85	90	95
w^s_{CA} / Ma%	3	3	2	3	3	2
w^s_{B} / Ma%	12	7	3	12	7	3
w^s_{CA}/w^s_{BCA} / %	20	30	40	20	30	40
ϵ / Vol%	45	35	20	45	35	20

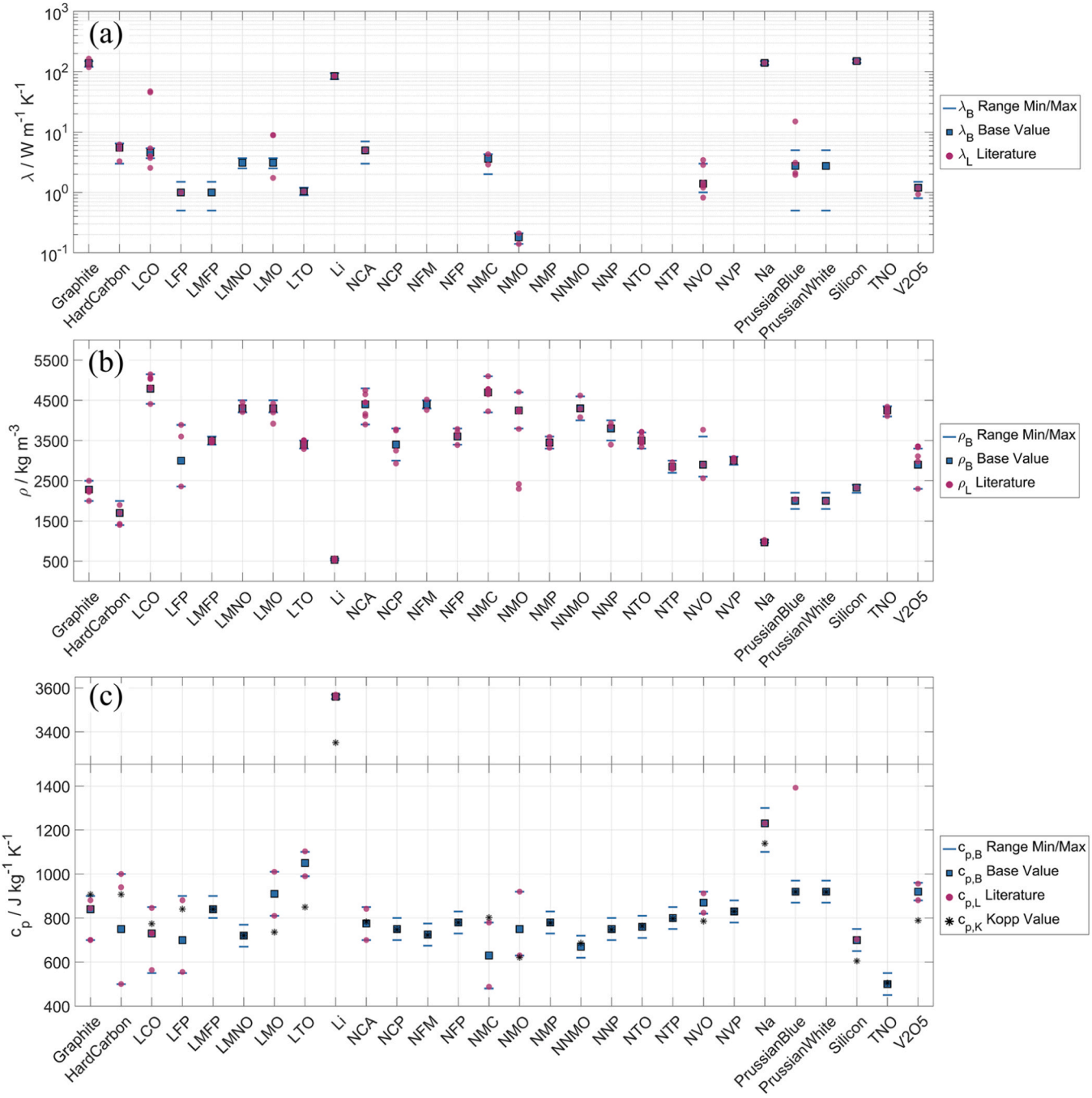

Fig. 2. Overview of literature values ●, selected base □ and limit values ▬ *as well as the calculated Kopp values* ✱ for (a) the thermal conductivity, (b) the density and (c) the specific heat capacity of active materials for lithium- and sodium-ion batteries.

$$c_{p,AM} = \frac{\sum_i N_i \cdot \tilde{c}_{p,i}}{\sum_i N_i \cdot \tilde{M}_i} \tag{3}$$

Fig. 2(c) also shows the calculated specific heat capacities according to Kopp. A comparison of the calculated values with the data from the literature shows that in many cases the calculated values according to Kopp are a very good approximation.

While comprehensive data based on literature values and databases is available for density, the data available for thermal conductivity and specific heat capacity is significantly more limited. For the latter, the Kopp calculation [151] is a suitable approximation method, as the values determined for numerous active materials are within the range of typical literature values. The limited availability of data on thermal conductivity is also due to the methodologically challenging characterization of particulate bulk materials. Overall, the data available on the thermophysical properties of battery materials, especially with regard to technologically relevant systems of the future, must be considered insufficient. Design variations at the electrode level further expand the spectrum. Simulative variation studies are intended to identify possible ranges of effective thermal properties and sensitivities of influencing factors on battery electrodes.

Determination of effective thermal parameters of the electrodes

The effective values for the electrode coating can be determined based on the data for the pure substances of the active materials, the

conductive additive, the binder, and the pore medium. In the variation studies, both the respective mass fractions of the solid phase and the pure substance data for the thermophysical parameters are varied. To calculate the effective value of the electrode, the pore volume is assumed to be completely filled with electrolyte and parameterized accordingly.

Calculation of the effective density and heat capacity of battery coatings

The effective density of the electrode coating $\rho_{C,eff}$ is determined by Eq. (4) by summing the volume-weighted individual densities of the electrode components.

$$\rho_{C,eff} = \sum_i \phi_i^{El} \cdot \rho_i \tag{4}$$

Analogous to the density, the effective specific heat capacity of the electrode coating $c_{p,C,eff}$ is determined by the mass-weighted summation of the individual specific heat capacities. The conversion of the mass fractions into volume fractions is done via the density of the individual components and leads to the following Eq. (5).

$$c_{p,C,eff} = \sum_i w_i \cdot c_{p,i} = \frac{\sum_i c_{p,i} \cdot \phi_i^{El} \cdot \rho_i}{\sum_i \phi_i^{El} \cdot \rho_i} \tag{5}$$

Determination of the effective thermal conductivity of battery coatings

The calculation of the effective thermal conductivity is more complex compared to the volume and weight fractioned-based analytical calculation for the density and specific heat capacity. Combining materials with thermal conductivities that differ by several orders of magnitude and a microstructure with complex heat conduction paths doesn't allow an easy and only volume-fraction based analytical calculation. In this work, the effective thermal conductivity of selected systems is determined using a 3D model approach with a heterogeneous resolution of the electrodes. An analytical model developed in our group, which is derived from the numerical model and was validated for material systems of established LIB [14,15,154], is used for the calculation during variation studies due to its computational efficiency.

Analytical model

The analytical determination of the effective thermal conductivity of the porous structure of battery electrodes is based on the model according to Oehler [15], which is a battery-specific extension of the Zehner-Bauer-Schlünder model [155–157] for porous particle beds. The calculation of the effective thermal conductivity of the electrode coating $\lambda_{C,eff}$ using the analytical model approach requires knowledge of the volume fractions of the individual components ϕ_i and the thermal conductivities of the pure substances λ_i. Additionally, two geometric parameters that describe the particle contact area α and the mean length of the binder phase between particles c has to be defined. In this study, the contact area between two active material particles is assumed to be zero, while the factor c used to describe the binding phase between two particles is calculated according to Eq. 7. The dependency is summarized in Eq. (6).

$$\lambda_{C,eff} = f(\phi_{AM}; \phi_{CA}; \phi_B; \varepsilon; \lambda_{AM}; \lambda_{CA}; \lambda_B; \lambda_{Med}; c; \alpha) \tag{6}$$

$$c = 0.008 \cdot \exp[4.21 \cdot \epsilon] \tag{7}$$

The effective value of the thermal conductivity of the battery electrode coating is determined by Eq. (8) based on the combination and weighting of three main heat conduction paths connected in parallel. These paths describe the heat transfer through the fluid and active material phases, as well as through a mixed phase of fluid, active material and binder-conductive additive (BCA) with the normalized radii r of the individual phases.

$$\lambda_{C,eff} = \left(1 - {r_2}^2\right) \cdot \lambda_{path1} + \left({r_2}^2 - {r_3}^2\right) \cdot \lambda_{path2} + {r_3}^2 \cdot \lambda_{path3} \tag{8}$$

The thermal conductivity of the additive phase consisting of binder and conductive additive is considered homogeneous for both models and calculated as the effective thermal conductivity of the BCA phase according to Hamilton and Crosser [158] using Eq. (9). As a factor, the value of $f = 3.2$ was used, as recommended by Oehler [154].

$$\lambda_{BCA} = \lambda_B \cdot \left[\frac{\lambda_{CA} + (f-1) \cdot \lambda_B - (f-1) \cdot \phi_{CA} \cdot (\lambda_B - \lambda_{CA})}{\lambda_{CA} + (f-1) \cdot \lambda_B + \phi_{CA} \cdot (\lambda_B - \lambda_{CA})} \right] \tag{9}$$

For a more detailed description of the analytical model by Oehler et al. and its validation for established LIB materials we refer to the corresponding publications from our group [14,15,154].

Based on the pure substance data, the electrode composition, microstructure parameters and the calculation Eqs. (4), (5), (6) and (8), the effective values for the thermal conductivity, density and specific heat capacity of the electrode coating are determined. In order to systematically investigate the influence of possible material and design variations in the configuration of battery electrodes, the analytical approaches described were used to determine not only a value based on the data of the defined base configuration, but also the influence of individual parameter variations and combined parameter variations that build on each other. The results obtained from these variation studies were summarized in scatter diagrams showing possible ranges of the effective thermal transport properties dependent on composition and individual material properties.

Fig. 3 shows an example of such a scatter plot for the thermal conductivity of an electrode coating with graphite as active material. The base configuration is based on the mean values for the volume fractions in Table 2 and the individual parameters of the pure substance properties in Table S4. Starting from the base configuration, individual parameters are adjusted stepwise, accumulation subsequently on each other, increasing or decreasing the effective thermal conductivity, resulting in the green and red lines. The objective of this variation is to identify possible maximum and minimum effective thermal conductivities based on variations of the electrode composition (ϕ_{AM}, ϕ_B/ϕ_{CA}, ϵ) and the thermal properties of the pure substances of active material (λ_{AM}), conductive additive (λ_{CA}) and binder (λ_B). The calculation is based on defined solid mass fractions and a defined pore volume fraction of the electrolyte phase. The BCA phase serves as the closing condition when varying the composition and is specified in the respective adjustment step with a constant composition ratio of binder and conductive additive. As already mentioned, the thermal properties of the electrolyte were not varied in this study for reasons of comparability. In order to also evaluate the individual influence of each variation variable on the thermophysical properties of the electrode coating, the single-parameter influence is shown in the black bars for the case of the base configuration.

With the aim to investigate the possible ranges of thermophysical parameters, the determination of effective thermal conductivity was chosen as the basis for the whole variation study. This is motivated by the very limited data available for this parameter and to overall gain a coherent dataset of thermal conductivity, density and specific heat capacity based on the same variation of the electrode composition. The parameter variation for effective density and specific heat capacity were therefore then carried out on the same basis concerning the electrode composition. Analogous to the determination of the effective thermal conductivity, calculations were made for the effective density and specific heat capacity so that the parameters for all three effective thermal parameters were varied, resulting in a coherent set of parameters. An excerpt of the scatter diagrams for an NMC electrode can be found in Section 4.1 in Fig. 7 while the summary of all scatter diagrams is provided in the supplementary section S5.

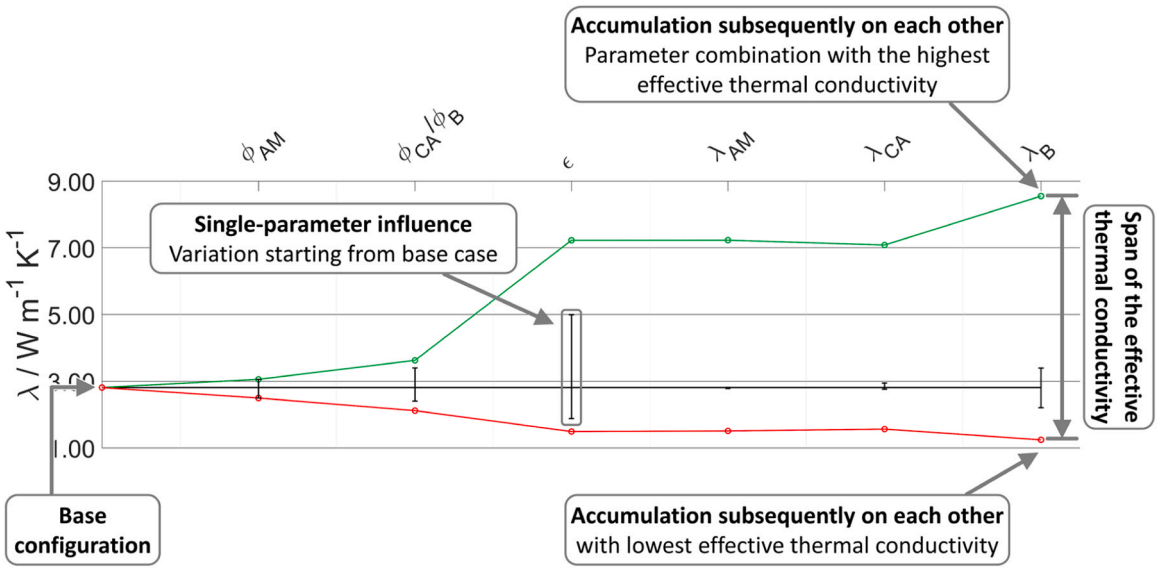

Fig. 3. Representation of the influence of parameters on the effective value using the example of the thermal conductivity of an electrode coating with graphite as active material with the help of a scatter diagram.

Numerical simulation

The numerical evaluation of the effective thermal conductivity of a heterogeneous resolved battery electrode presented in this work involves three steps. In the first step the particular microstructure of the active material is replicated in MATLAB using a stochastic Drop- and Roll algorithm. In the next step the binder-conductive-additive-phase (BCA) is added to the active material phase. The last step is the transfer of the geometry objects to COMSOL Multiphysics, parameterize and mesh them, set the initial and boundary conditions and simulate the heat transfer. The heterogeneous replication of the microstructure of a battery electrode coating is based on a modified in-house generic geometry generation routine which is presented in previous publications by Oehler et al. [14,15,154] and Seegert [159]. The microstructure generation routine was adapted and further developed as a part of this work, and instead of using the open-source tools OpenSCAD (computer aided design (CAD) program) and OpenFOAM (finite volume method (FVM) simulation tool) in the work of Oehler et al., the software COMSOL Multiphysics (finite element method (FEM) simulation tool) in combination with MATLAB was used. To distinguish enhancements in the generation routine for microstructures from the approach in our previous work, we will explain the routine and describe the corresponding adjustments.

First a matrix is generated that contains all geometric information about the graphical objects, that represent the desired active material configuration. According to the corresponding probabilities of a particle size distribution (PSD), the entries of the volume-equivalent diameters are entered into the matrix and sorted randomly. The shape of the active material particles, can be modified to ellipsoids or super-ellipsoids in order to better replicate real electrode microstructures or to investigate the influence of the particle shape itself. Eq. (10) is used to calculate the semi-axes of an ellipsoid with the same volume as the corresponding sphere with the specified diameter from the PSD. In this case a, b and c are the corresponding half-axis, r is the volume-equivalent radius from the PSD and w_x, w_y and w_z are the aspect-ratios to modify the sphere to an ellipsoid, which is shown as an example in Fig. 4. This also ensures that the PSD is maintained when the particles are modified. Furthermore, several aspect-ratios with corresponding probabilities can be specified. The assignment to the respective particles is random in this case. In addition to modifying the shape of the graphical objects, also their initial rotation can be defined.

$$\begin{bmatrix} a \\ b \\ c \end{bmatrix}_i = \frac{r_i}{\sqrt[3]{w_x \cdot w_y \cdot w_z}} \cdot \begin{bmatrix} w_x \\ w_y \\ w_z \end{bmatrix}_j \tag{10}$$

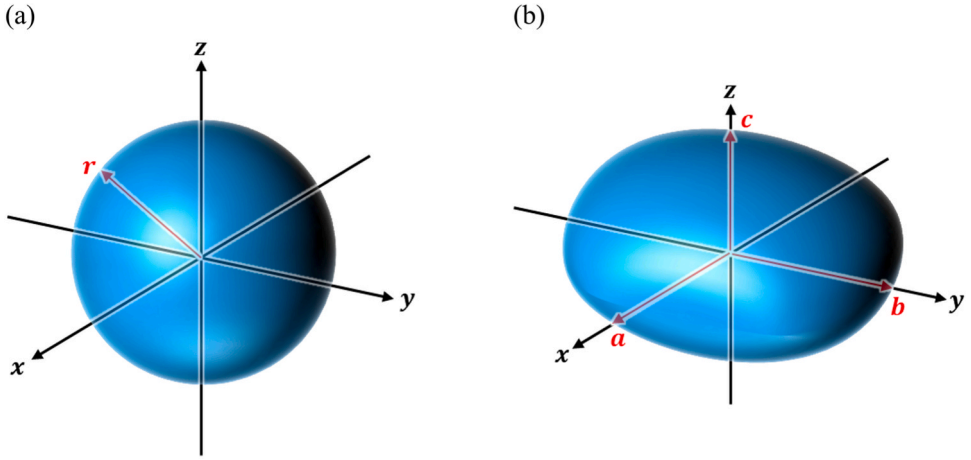

Fig. 4. Comparison of a (a) spherical geometric object with an (b) ellipsoid derived using given aspect ratios.

After defining the stochastic distribution based on the desired electrode configuration, the graphical objects are sedimented one after another in a predefined system volume until they reach a stable position. In order to obtain a random distribution in the particle bed, the input variables for the PSD, aspect ratios, and initial rotation are randomly combined with each other. The system volume is defined by a base area in x- and y-direction and a height in z-direction. The particles are generated randomly in the system volume and move in negative z-direction by a predetermined increment unit until they either reach the lower system limitation or get in touch with other particles which are already positioned. If they get in contact with each other, the graphical object is rotated by predefined Euler angles around the center of the shape to ensure the particle reaches a stable position. This is achieved when no further movement is possible without particle intersecting. For this purpose the Gilbert-Johnson-Keerthi algorithm by Gilbert et al. [160]. is implemented and checks whether there is contact between two geometric elements during each step. After reaching a stable position, the next particle is generated until the upper system limitation is reached. Particles that come into contact with the lower boundary ($z = 0$), which corresponds to the current collector, are cut off by a predefined length to ensure a desired contact area between the system boundary and the particles. If a particle crosses one of the four outer lateral boundaries of the system volume during the sedimentation, the particle is cut and the section is mirrored on the opposite side. Like the cutting off of the particles at the lower boundary a similar procedure takes place at the upper limitation of the system volume. Particles that exceed over the upper limitation corresponding to the separator are cutting off to ensure a contact area and to terminate the sedimentation process when a particle protrudes beyond the predefined value.

After ending the sedimentation process all structural data like particle size, half-axes, cartesian coordinates and the rotation of each particle are transferred to COMSOL Mutiphysics via the MATLAB-COSMOL-Livelink to rebuild the structure and evaluate the volume fraction and specific surface area of the active material structure. According to the generation of the BCA-domain later in this process and the meshing and simulation afterwards, it should be mentioned that the half-axes of the particles are multiplied with a shrink factor to avoid point contacts and reduce narrow regions. This reduction in the length of each half-axis by less than two percent has a negligible effect on the particle size distribution. This factor can also be used in combination with the drop-and-roll algorithm to reduce the volume fraction of active material in the system e.g. the replication of high porous electrodes. In order to still achieve the predefined particle size distribution, this is first shifted to higher total values and then reduced to the original size distribution. This results in a greater distance between the particle centers and, consequently, higher porosity and a lower active material volume fraction.

According to the previous work [14,15,154,159] the generation of the Binder-Conductive-Additive-Domain takes place after the generation of the particular microstructure of the active material phase. The assumption of a homogenized phase consisting of binder and conductive additive has already been shown and is justified by the accumulation of these two phases into clusters as shown by Pfaffmann et al. [161]. The design of the BCA-Phase as shells around or as bridges between active material particles adapted in the routine in COMSOL in this work is similar to the previous work from our group.

The generation of BCA-shells refers to the defined volume fraction, an initial relative factor corresponding to the particle diameter, and a probability. The outer shell diameter is calculated by multiplying the diameter of the individual particle with the relative factor. The defined probability determines whether a shell is created or not. For example, a probability of 50 % means every second particle has a binder shell. Afterwards the geometry elements are then transferred to COMSOL and the volume fraction of the binder shells is determined. In order to correctly determine the volumes of the individual phases, overlapping geometric elements are subtracted from each other. The process of the creation of a shell is shown in Fig. 5(a) to (c). If the evaluated volume fraction of the shells mismatches the defined value, the relative factor is either in- or decreased to raise or reduce the volume fraction of the shells. This is repeated until the value lies within a certain fluctuation around the predefined value. Generating BCA-bridges between two particles follows a similar routine. In addition to the probability of generating a bridge, two relative factors are defined depending on the diameters of the particles involve, one for the permissible bridge length and one for the bridge radius. To fulfill the condition whether a bridge may be generated, for each couple of particles in the system the distance between the center points is evaluated. If the calculated bridge length is within the permitted bridge length, it will be created. Once all possible bridges have been identified, the probability of creating a bridge is also taken into account here. After determining the bridges, the geometry elements are transferred to COMSOL to calculate the volume fraction of the BCA-bridges. The bridges are approximated in COMSOL as cylinders between the particle centers. Analogous to the previous step, the intersection between the active material particles and the shells are subtracted and only the volume of the bridges is evaluated. Fig. 5(d) to (f) shows the generation process of a bridge between two active material particles. If this doesn't match the defined value, either the bridge length or the radius can be in- or decreased. This iteration of either the length or radius is executed until the predefined value of $\pm$ 0.5 Vol% is reached. There is also the option of producing only shells or bridges, or a combination of both according to predefined volume fractions, as shown in Fig. 5(g) to (i). It is also possible to grade the BCA phase based on the height of the electrode, for example, to replicate binder migration. The simulation of the BCA phase using the simplified representation of shells and bridges shows good agreement for the determination of effective thermal conductivity, as proven in previous studies. The validation studies shown in Supplementary Information S7 compared with experimental data confirm this. For better comparability and in line with previous work by our group [15] this study also focuses primarily on binder bridges for BCA phase generation, resulting in an overall BCA network throughout the electrode.

After finishing the structure generation process all geometry elements are finally transferred to COMSOL Multiphysics. To simplify the parameterization of the individual geometry objects, the phases of the active material and the BCA are each combined into a union. The remaining pore volume is defined as the electrolyte phase. All necessary variables and parameters are then implemented and assigned to the corresponding phases. To evaluate the effective thermal conductivity of the electrode replica, the physics module "Heat Transfer in Solids" in COMSOL is used. For the lateral system boundary, "Thermal Insulation" is selected as an adiabatic boundary condition. A first-order boundary condition with a fixed temperature value is specified at the lower (323 K) and upper (273 K) system limit. A schematic representation of the boundary conditions is shown in Fig. 6(b) using a polydisperse spherical active material. The arithmetic mean value of these two temperatures (298 K) is selected as the initial value for the whole structure. Once the physics module has been implemented and the initial and boundary conditions are defined, the mesh is added. The geometry is meshed using "Free-Tetrahedral" for each of the phases, shown in Fig. 6 (c). Following the mesh-generation, a study is implemented using a stationary solver. Fig. 6(d) shows an example of the temperature distribution across the microstructure. The model is setup completely automatically using the MATLAB-COMSOL-Livelink.

To validate the improved microstructure generation routine, the electrodes of a high-power 3.2 Ah KOKAM cell presented and experimentally characterized by Oehler [14] were replicated. The results are summarized in Supplementary Information S7 and show a deviation of a maximum of 12 % for both electrodes, which is within the margin of measurement accuracy.

In addition to the representation of spheres and ellipsoids, which can be chosen as a good approximation for most electrode structures of commercial LIBs, the microstructure simulation was expanded to better

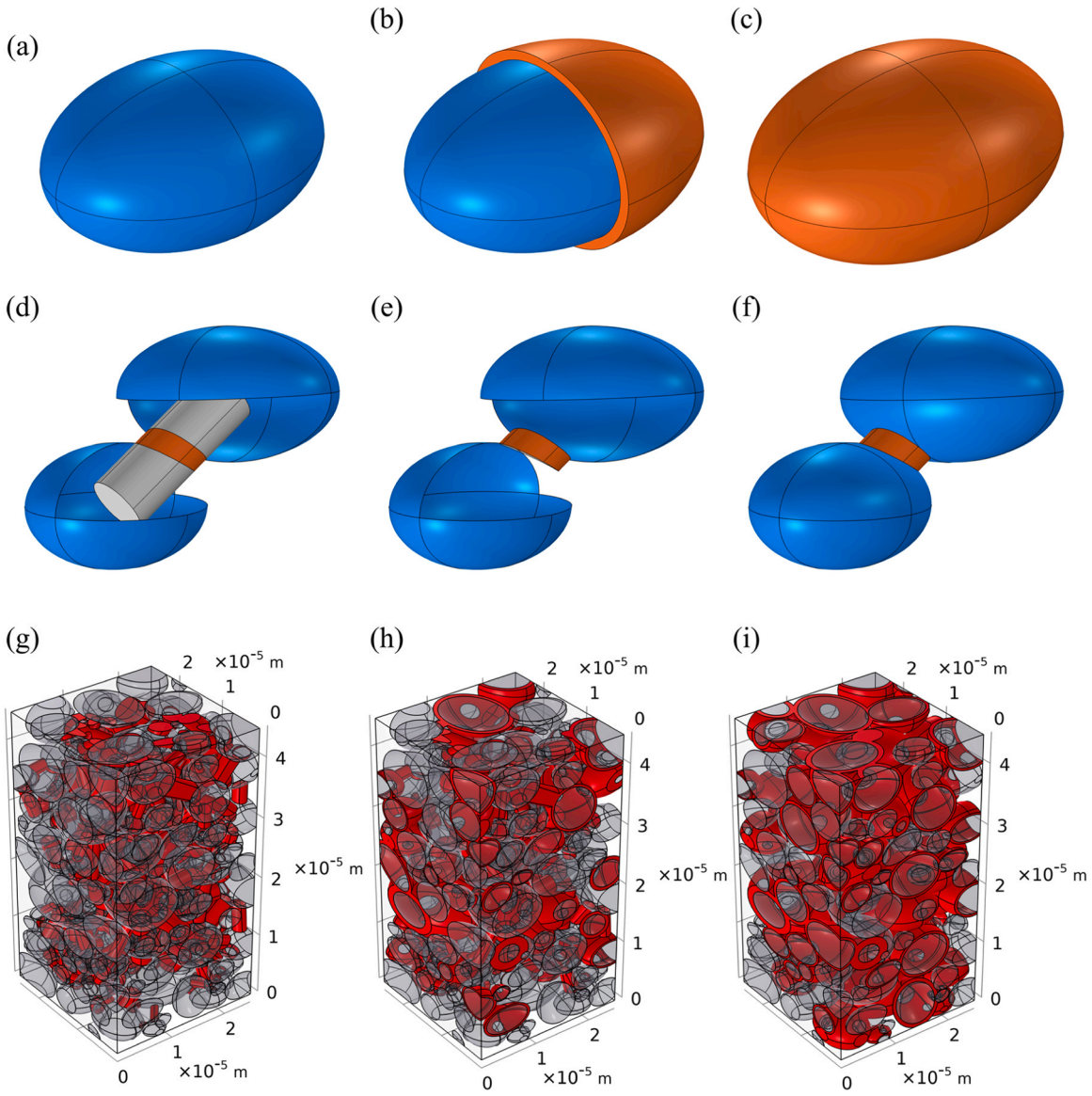

Fig. 5. An (a) ellipsoid-shaped active material (b) the cross-section view of a BCA-shell and (c) the full BCA-shell around the active material particle. (d) shows a BCA-bridge between the center of two active material particles (e) the remaining bridge after subtracting the intersecting parts and (f) the final bridge between the two active material particles. (g) shows a structure with only BCA-shells, (h) a combination of shells and bridges and (i) a structure with only BCA-bridges.

simulate NIB systems in the future. This was done against the background that Prussian blue and its analogues, as well as Prussian white, have cube-shaped active material particles [162]. Against this background, the generation routine in MATLAB was extended to include graphics object generation based on the equation according to Barr [163] for super ellipsoids. If $n = m \gg 10$ is selected for the values of the exponents in the equation, as shown by Becker [164], cube-shaped geometry objects can be generated in MATLAB. The methodology for microstructure generation is analogous to that for spherical particles. The geometry elements are then transferred in COMSOL using block elements instead of ellipsoids, while the remaining automated model set-up process stays the same. A corresponding replica of the microstructure for a Prussian blue electrode with cube-shaped active material particles is shown in Fig. 11 in Section 4.

Evaluation of the effective thermal conductivity

In this section, the calculation of the effective thermal conductivity for porous media is explained. In solids and static liquids, a temperature gradient induces heat transfer trough thermal conduction. COMSOL uses the transient heat conductive equation extended by the convection and source term shown in the following Eq. (11). Where T is the temperature, t is the time, $\vec{u}$ is the velocity field, $\dot{Q}_S$ is the source term and V the volume. The material-specific variables ρ, c_p and λ are the density, specific heat capacity and thermal conductivity.

$$\rho \cdot c_p \cdot \left(\frac{\partial T}{\partial t} + \vec{u} \, \nabla T \right) = \nabla (\lambda \cdot \nabla T) + \frac{\dot{Q}_S}{V} \tag{11}$$

The implemented equation uses the resolved form with the definition of the Fourier heat conduction Eq. (12). Assuming isotropic material properties, this leads to the following Eq. (13) rearranged according to the source term.

$$\vec{q} = -\lambda \cdot \nabla T \tag{12}$$

$$\frac{\dot{Q}_S}{V} = \rho \cdot c_p \left(\frac{\partial T}{\partial t} + \vec{u} \cdot \nabla T \right) + \nabla \cdot \vec{q} \tag{13}$$

Since the effective thermal conductivity is to be derived from the structure, neither heat sources nor sinks are taken into account in the

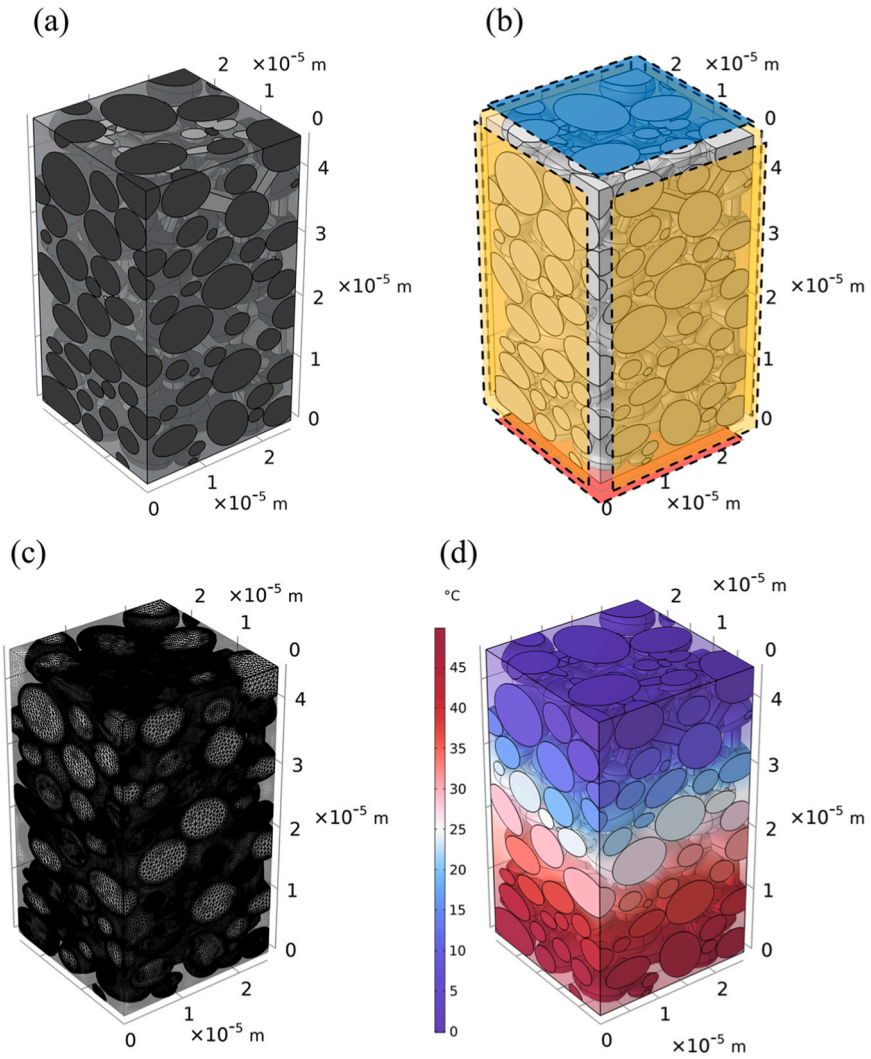

Fig. 6. (a) The electrode replica, (b) Microstructure with schematic representation of boundary conditions – red: 323 *K*, blue: 273 *K*, yellow: adiabatic, (c) meshed microstructure and (d) the stationary solution of the temperature distribution across the microstructure and.

structure, and no flowing medium is involved, so that the source and convection terms are set to zero. This leads to the following Eq. (14), which corresponds to the transient heat conduction equation in its original form.

$$0 = \rho \cdot c_p \frac{\partial T}{\partial t} + \nabla \cdot \vec{q} = \rho \cdot c_p \frac{\partial T}{\partial t} - \nabla \cdot (\lambda \cdot \nabla T) \tag{14}$$

To find the solution to this equation, the Fourier heat conduction term must be solved. Since only one-dimensional heat transfer in the z-direction needs to be solved and the stationary solution is of interest, the equation simplifies to the following form Eq. (15) of the Fourier's equation.

$$\dot{q} = -\lambda \frac{\partial T}{\partial z} \tag{15}$$

The total heat flow is obtained by integrating the heat flow over the base area A of the structure which leads to the Eq. (16) for the total heat flow $\dot{Q}$.

$$\dot{Q} = \int_A \dot{q} \cdot \vec{n} \, dA = -\int_A \lambda \frac{\partial T}{\partial z} \cdot \vec{n} \, dA \tag{16}$$

To derive the effective thermal conductivity λ_{eff} of the structure with Eq. (17), the evaluated total heat flow relative to the total base area is calculated using the temperature gradient ΔT across the height H of the structure.

$$\lambda_{eff} = -\frac{\dot{Q}}{A} \frac{H}{\Delta T} \tag{17}$$

Results and discussion

Variation study of thermophysical properties of battery electrodes

The outcomes of the investigation into potential material and design variations in the configuration of battery electrodes described in Section 3 are summarized in Fig. 8. The effective values shown for the thermal conductivity, density, and specific heat capacity of the electrode coatings are based on the derived scatter diagrams and are compared for the different battery materials investigated. In addition to the value for the base configuration, the respective end values after the variation for the lower and upper configuration are also depicted. As explained in Section 3, the variation was carried out with the aim of adjusting the electrode configuration within plausible limits, starting from a base value, so that this results in a maximum and minimum effective value for thermal conductivity. In order to obtain a consistent data set for the three thermal properties, this variation of the electrode configuration is also used as the basis for calculating the effective density and specific heat capacity. Fig. 7 shows the corresponding scatter diagrams for a NMC

electrode.

For the effective thermal conductivity and density, the picture is similar, with higher proportions of electrochemically active components leading to higher effective values for the overall electrode. For the effective specific heat capacity, the picture is mostly reversed. The parameter configuration that delivers the highest effective values for thermal conductivity and density often results in a value below that of the base configuration in case of specific heat capacity. This can be explained by looking at the input parameters in S4a and S4b, which serve as the basis for calculating the effective values of the electrodes. The thermal conductivities of the electrochemically inactive components (binder and pore medium) are significantly lower than those of the active materials.

The proportion of conductive additive in the overall system is too small to have a significant influence on the entire system if, for example, the total proportion of the binder-conductive additive (BCA) phase increases. A closer look at the individual scatter diagrams in Fig. 7 and in the supplementary S5 reveals that the most significant influencing parameter for the effective thermal conductivity is the porosity of the overall electrode; a higher solid content leads to higher effective values, which supports the previous statement. As the pure substance value of the thermal conductivity of the active material increases, and consequently the effective value of the electrode increases, the influence of the active material on the effective thermal conductivity of the overall electrode decreases since the other components impede the heat transfer. This becomes particularly clear when considering graphite and silicon as active materials, which both have comparably high thermal conductivities and variation of their pure substance properties show almost no influence on the overall thermal conductivities of the resulting porous electrode. On the other hand, the influence of variation of the active material properties is very significant for active materials with comparably low thermal conductivity, such as NMO, LTO, or LFP. The thermal conductivity of the binder and the content of conductive additives in the BCA phase have a similar influence to the previously described effects of the active material. As the thermal conductivity of the active material increases, the importance of the binder and conductive additives for the effective electrode properties rises. This clearly shows which component limits heat transport through the electrode structure and provides a comprehensive picture.

Graphite and hard carbon have become established as commercially used materials in LIB and SIB, especially for anode systems, which greatly reduces the variety of active materials [7,165]. The picture is different for the cathode side, with a wide range of active materials available. Despite the variety of materials for cathode systems, the

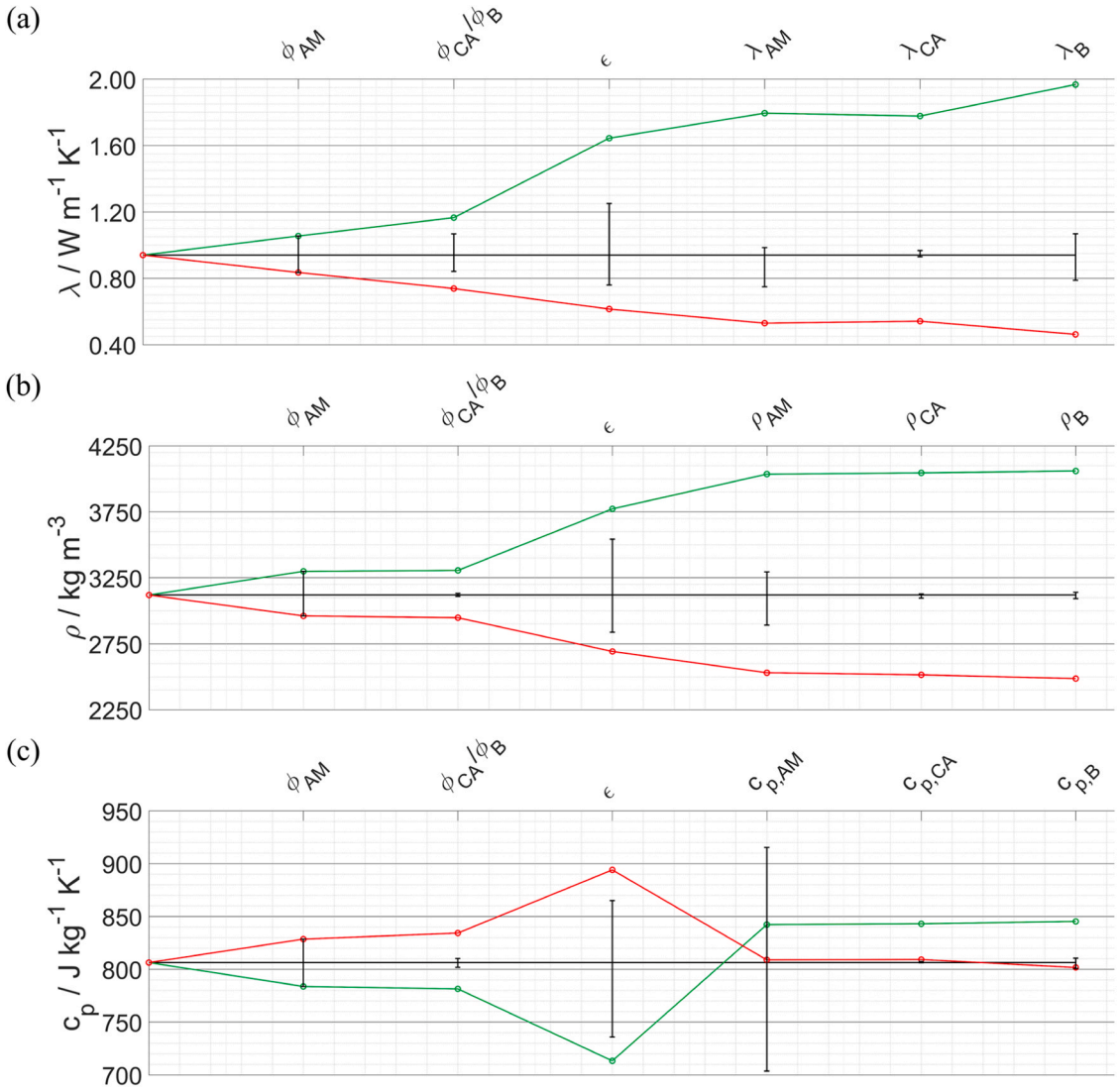

Fig. 7. Excerpt from the determination of effective values for an electrode with NMC as active material with (a) thermal conductivity, (b) density, and (c) specific heat capacity, shown as a scatter plot with the underlying dependencies of composition and individual material influence.

effective thermal conductivity for LIB and SIB electrode coatings averages 0.75 ± 0.25 Wm^{-1} K^{-1} for layered oxide, olivine, and cubic structures. These results are consistent with experimentally determined values from Spitthoff et al. [9], Steinhardt et al. [8], and Marconnet et al. [12]. A difference in the active materials examined here between LIBs and SIBs is not apparent, although the data available is insufficient, particularly for SIB systems. Most anode systems result in a slightly higher effective thermal conductivity compared to cathode systems, due to the significantly higher thermal conductivity of the active materials.

A similar picture emerges for the calculation of the effective density of the electrodes. Here, too, porosity and, as a result, the total solid fraction are shown to be the strongest influencing parameters on the effective value of the electrode coating. Since the densities of the electrochemically inactive and active components are similar for most materials, the volume fraction of active material and its density are the next most important influencing factors on the effective value, alongside the total solid content. Since the total proportion of active material in the electrode is significantly higher than that of the BCA-phase, the active material results in higher sensitivity to the effective value of the electrode. The effective density values are higher for cathodes than for anodes, with LIB systems tending to have slightly higher values than SIB systems.

As already mentioned, the situation is different when it comes to the factors influencing the effective specific heat capacity. The progression of the configuration's changes compared to those of effective thermal conductivity and density. This is due to the higher specific heat capacity

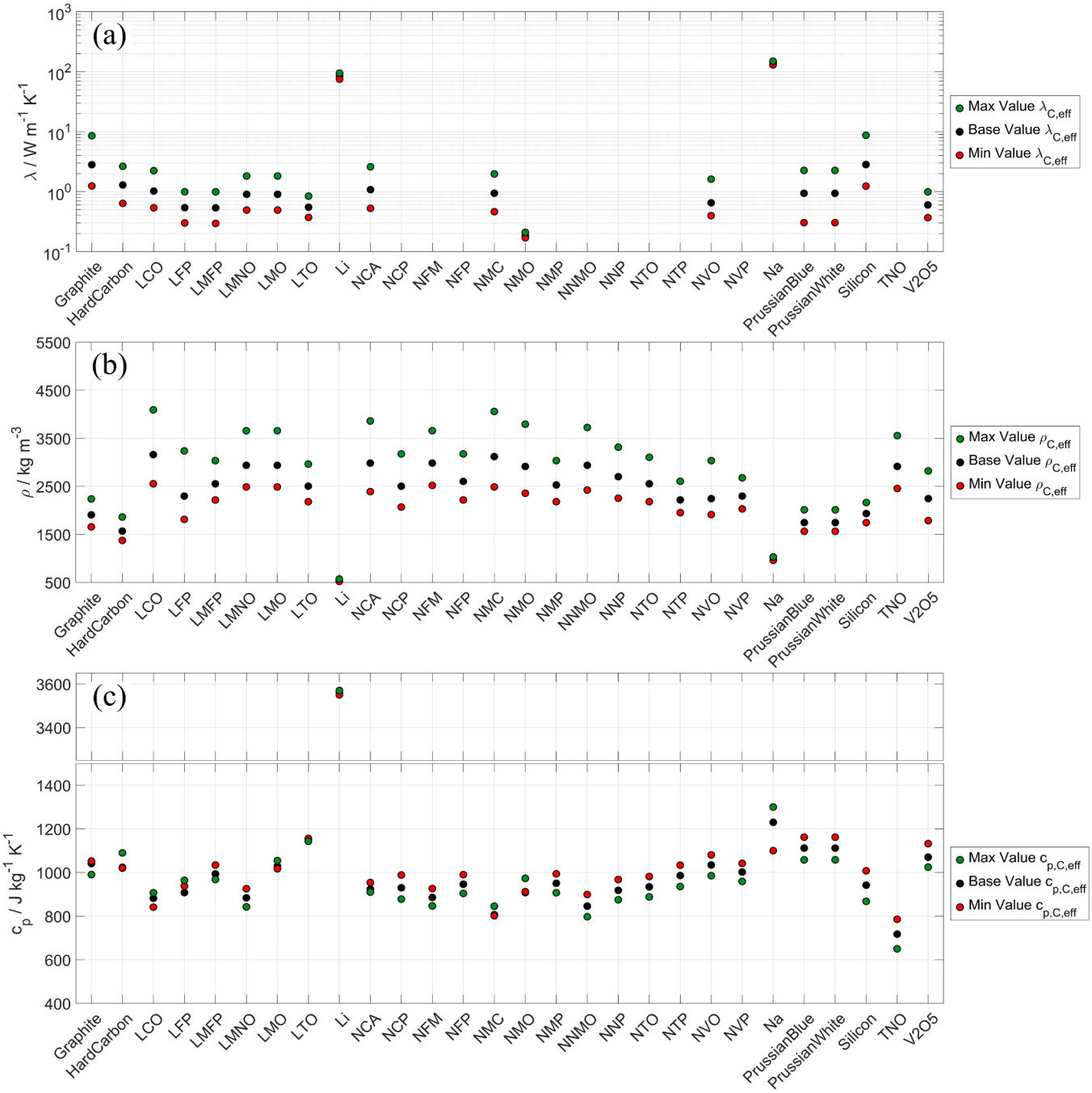

Fig. 8. Overview of the calculated effective electrode values with the base and the end values for (a) the thermal conductivity, (b) the density and (c) the specific heat capacity for LIB and SIB.

of the electrochemically inactive components binder and electrolyte compared to the active materials. As with effective thermal conductivity and density, the most decisive factors are the porosity and the specific heat capacity of the active material. A detailed look at Fig. 7 and the scatter diagrams in S5 also shows that the porosity and the underlying values for the specific heat capacity of the active material have opposite effects on the effective value of the electrode coating. This is particularly evident in the configurations for NMC and NMO. However, as in the other two diagrams, the graph in Fig. 8(c) also shows the final value based on the variations chosen for the determination of the effective thermal conductivity, in this case, not the maximum or minimum value, in order to obtain a coherent data set. The individual variations show, as can be seen in Fig. 7, that a larger effective value range is theoretically possible for the specific heat capacity. The overall trend here is the opposite of that for density, and the specific heat capacity for cathodes is lower than that for anodes, although it is difficult to distinguish between LIB and SIB systems. The difference is slightly greater for density than for heat capacity, so that the volumetric heat capacity follows the trend of density.

In summary, it can be noted that the porosity and, conversely, the solid content of the electrode have the greatest influence on the effective values of all thermophysical properties of the electrode coating. The change in the effective value as porosity varies within the specified limits depends on the initial value. For thermal conductivity, graphite and silicon show an increase in the effective value of approximately 77 % when porosity is reduced to 20 Vol% and a decrease of just under 33 % at a porosity value of 45 Vol%. Since most cathode active materials exhibit similar initial values for effective thermal conductivity, their dependence on porosity also shows an increase in the effective value of approximately 20–35 % or a decrease of 13–20 %. A similar trend is observed for density, with an increase of 4–14 % (porosity reduced to 20 Vol%) or a decrease of 2–9 % (porosity increased to 45 Vol%.) in the effective value. Since the pure material values for the densities of the active materials under consideration do not differ by several orders of magnitude, as is the case with thermal conductivity, no single material stands out in particular here. For the effective specific heat capacity, no trend is observed as a function of the underlying effective value, and the fluctuation around the calculated value lies within a range of 2–10 %.

For thermal conductivity, the binder also proves to be a limiting component in the heat transport paths through the structure and is therefore sensitive in the effective value determination. Similarly to the symmetric variation in the thermal conductivity of the binder by ± 0.05 Wm^{-1} K^{-1} around the base value, the resulting effective value of the electrodes also varies by up to ±20 %. For the specific heat capacity, the highly sensitive influence of the pure substance properties of the active material on the effective value is particularly noteworthy, as it counteracts the influence of porosity. The effect on the effective value is of the same order of magnitude as that of porosity.

Comparison between analytical and numerical simulation

In addition to the influence of different variations on the effective values of the thermophysical parameters, the analytical model according to Oehler et al. [15]. for determining the effective thermal conductivity will be compared with the numerical model presented in chapter 3.2, and the results will be evaluated. For this purpose, defined cases for NMC, graphite, and Prussian blue electrode coatings are replicated and the results are compared with each other. A detailed list of the input variables for simulating such electrode structures can be found in supplementary section S6. A brief comparison of the results for the effective thermal conductivity of the electrode coating calculated using the analytical and numerical model compared to experimental data from the literature can be found in Table 3.

NMC configuration

The first case involves simulating the base configuration of the NMC electrode. The underlying particle size distribution is simulated based on data from NEI Corporation [166]. The particle shape of spheres used as a basis is justified by cross-section images such as those found in Pfeifer et al. [13]. The numerical simulation was performed on two differently stochastically distributed microstructures in order to demonstrate the reproducibility of the results. After their creation, both structures show good agreement with the predefined volume fractions but are composed of a locally different distribution of active material particles and BCA-phase. The comparison is made with the values for effective thermal conductivity determined using the model according to Oehler et al. [15]. With values of 0.94 Wm^{-1} K^{-1} and 0.95 Wm^{-1} K^{-1}, both structures shown in Fig. 9 show a deviation of 0.28 % and 1.37 % from the analytically determined values and, consequently, a very good agreement between the two models as well a very good replication of the representative electrode section with the two stochastically generated microstructures.

Graphite configuration

Compared to the NMC structure, the simplifying assumption of spherical active material particles in graphite electrodes is not justified. In this case, the AM phase is approximated using ellipsoids, as exemplified by SEM images in Asenbauer et al. [165]. The underlying particle size distribution was selected in the same way as for the NMC configuration based on data from NEI Corporation [167] and reconstructed using Origin 2023. The aspect ratio was selected in the same way as in the work of Oehler [14] and specified for microstructure generation on a proportionate basis. The heterogeneous replication of the electrode coating for the two simulation cases is shown in Fig. 10. A detailed overview of the PSD, aspect ratio, and thermophysical parameters for the calculation is provided in the supplementary section S6. Despite the good agreement between the volume fractions of the AM, BCA, and electrolyte phases, a direct comparison of the numerical and analytical simulations reveals a larger deviation of approximately 30% in the effective thermal conductivity between the analytical model based on spherical particle shape and the numerical models based on ellipsoids. As already discussed by Oehler [14], this is due to the underlying aspect ratio, which must be taken into account for heat transport through the microstructure. The compression of the semi-axis along the heat flow path results in an accumulation of heat transfer between the highly thermally conductive active material phase and the poorly thermally conductive BCA and electrolyte phases. Correcting the value of 2.81 Wm^{-1} K^{-1} calculated with the analytical model with spherical particle shape taking the proportion-weighted aspect ratio in the heat transport direction (z-axis) of 0.76 into account, results in a value of 2.13 Wm^{-1} K^{-1} for the effective thermal conductivity through the electrode. The deviation between the analytical and numerical models is reduced to just under 5% and 1%, respectively. This shows that the consideration of heat transport through the microstructure and the underlying aspect ratio of the active material particles is crucial here and must be taken into account, which is made possible by application of the heterogeneous microstructure simulation model.

Prussian blue configuration

As already presented in the section on the numerical model, microstructure simulation was expanded to include the aspect of generating cube-shaped active material particles, which are typical for Prussian blue and white active material particles [162]. As with the other electrode simulations, a particle size distribution from NEI Corporation [168] was selected for microstructure generation. Like the NMC and graphite structures, the specified volume fractions of the PB structure are also reproduced very well. The underlying data for the PSD and volume fractions can be found in the supplementary section S6, while the heterogeneous reproduction of the electrode structures is shown in

Table 3
Comparison of the effective thermal conductivity of electrode coatings with NMC, graphite, and Prussian blue as active material, determined using analytical (An) and numerical models (N1, N2) and compared with literature values (Lit).

Active material	Analytical λ_{An} / $Wm^{-1}K^{-1}$	Numerical 1 λ_{N1} / $Wm^{-1}K^{-1}$	Numerical 2 λ_{N2} / $Wm^{-1}K^{-1}$	Literature λ_{Lit} / $Wm^{-1}K^{-1}$
NMC	0.94	0.94	0.95	0.91 [169]
Graphite	2.13	2.22	2.11	1.8…2.8 [14,15]
Prussian Blue	0.94	1.08	1.08	–

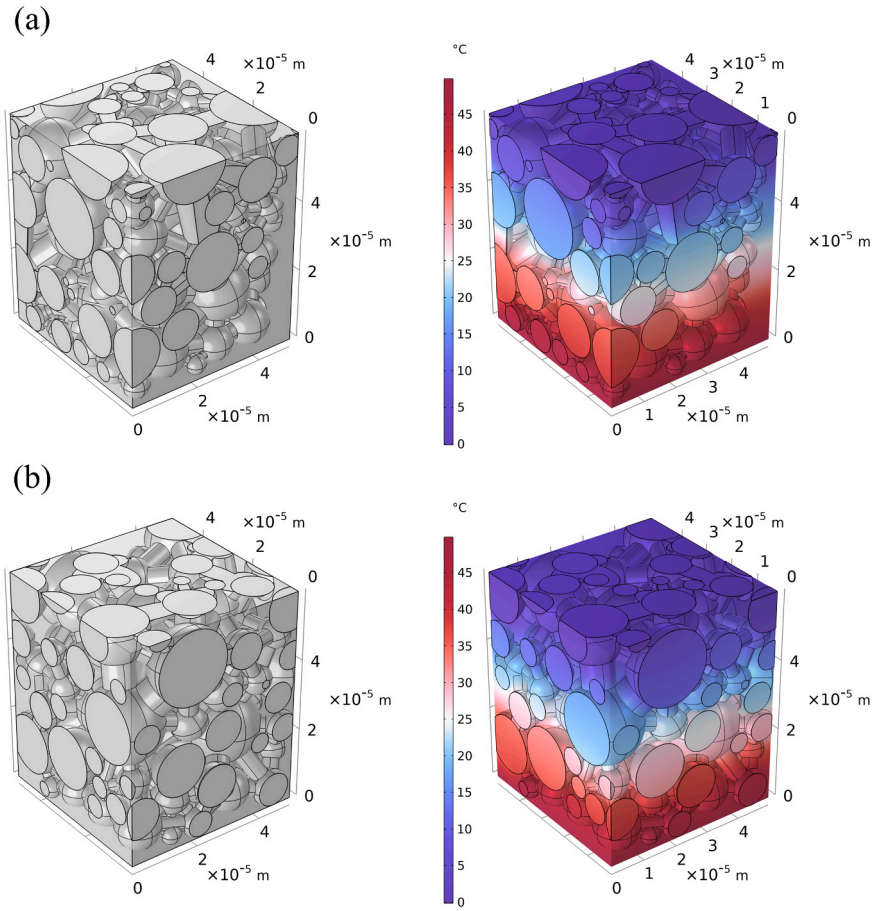

Fig. 9. Microstructure replication of generic NMC electrodes with spherical particles and polydisperse particle size distribution for two stochastically generated structures (a) and (b) with identical structural parameter specifications.

Fig. 11. In both cases, the effective thermal conductivity of the generic microstructure replication in the numerical simulation model is approximately 13 % higher than that of the analytical model. This is to be expected, since the calculation in the analytical model is based on spherical particles, which is not the case in the 3D microstructure replication. A correction factor for the calculation using the analytical model analogous to the aspect ratio as in the ellipsoid shaped graphite electrode, or, for example, a correction based on sphericity, does not lead to promising results in this case. Even replacing the geometric elements of the active material with spheres of identical diameter or equivalent volume does not provide a sufficient explanation for the given deviation between the numerical and analytical models Nevertheless, the value of 0.94 Wm^{-1} K^{-1} determined using the analytical model provides a good approximation compared to the value of 1.08 Wm^{-1} K^{-1} from the numerical model and, given the current poor data basis, provides a good starting point from which to make improvements and analyze influencing factors.

Overall comparison of heterogeneous electrode replication

For the electrode coatings reproduced here and the resulting thermal conductivities, summarized in Table 3, there is overall good comparability between the analytical and numerical models as well as the comparison with electrodes from the literature. It should be emphasized that the electrode coatings reproduced here are generic model cases. Comparison with literature values is only possible with certain limitations, as parameters such as the porosity or particle shape of the active material have a significant influence on the effective properties, and these vary greatly in the electrodes examined in the literature or are not always known. However, the models prove to be suitable for consistently reproducing the underlying relationships and show very good agreement with the values found in the literature.

Conclusion and outlook

The selection and composition of materials determine the effective thermal behavior from the electrode to the cell level of LIB and SIB, which affects the entire battery system, for example. The data available

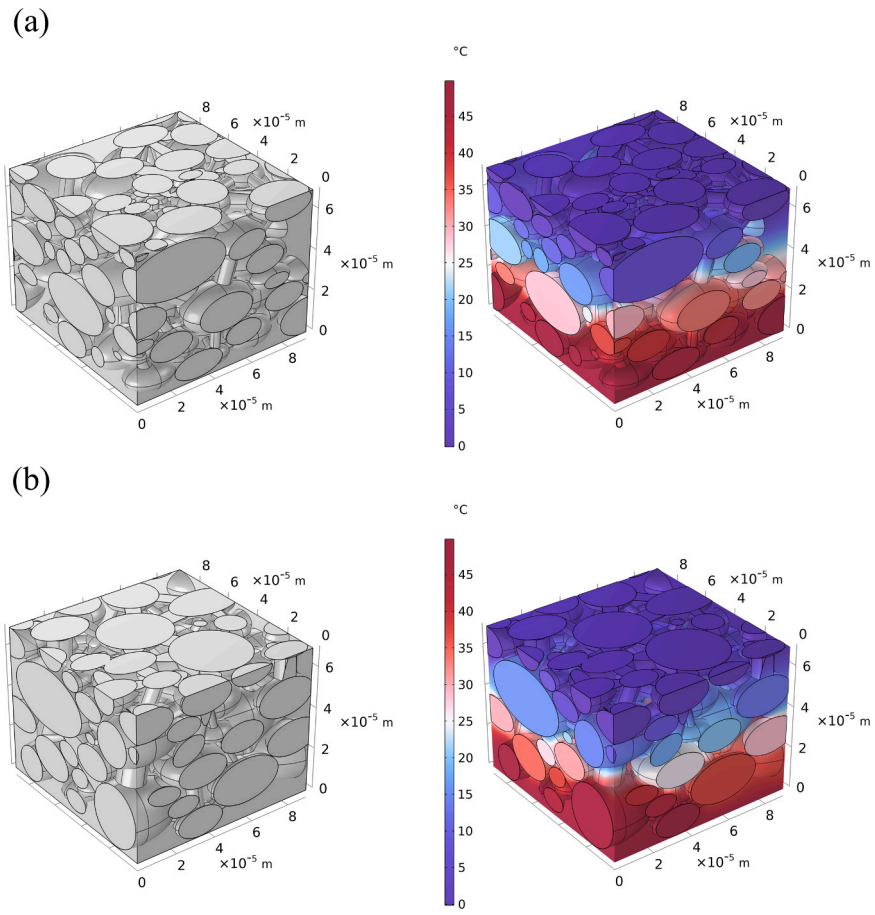

Fig. 10. Microstructure replication of generic graphite electrodes with ellipsoidal active material particles and polydisperse particle size distribution for two stochastically generated structures (a) and (b) with identical structural parameter specifications.

is very limited, especially for next-generation LIB and SIB. Against this background, extensive data from literature, material databases, and manufacturer specifications were compiled to provide a comprehensive overview of the available pure substance thermophysical parameters for active materials of lithium- and sodium-ion battery electrodes. The focus is on the thermal conductivity, density, and specific heat capacity of established and future technically relevant materials. While acceptable data could be found for density, including for possible future materials, this was only possible to a limited extent for specific heat capacity, and even less for the thermal conductivity of the active materials. In addition, a calculation approach according to Kopp was used to approximate the specific heat capacity, and its applicability was demonstrated by comparison with available data on established battery materials. The devised data set of pure substance constitutes the basis for determining the effective thermophysical properties of porous electrodes for the investigation of a broad spectrum of possible design variations in battery cells. For this purpose, a base value and a fluctuation range were defined for the respective materials based on the researched parameters. On the one hand, this is intended to provide a good base value, but on the other hand, due to insufficient data in the literature, it also takes into account influences such as different material and crystal configurations or temperature and state of charge dependencies. In addition to the pure material data and their ranges, also the electrode composition was defined based on data from commercial suppliers. To establish a basis for electrode design, the following three cases were defined: a base configuration, as found in typical technically advanced electrodes, an upper configuration with a higher AM content, and a lower configuration in which the share of AM is reduced.

In addition to the volume- and mass-weighted calculation of the effective values for the density and specific heat capacity of battery electrodes, determining the effective thermal conductivity poses greater challenges. This is due to the complex heat conduction through the underlying heterogeneous microstructure of the porous electrodes composed of active material particles, a connecting BCA-phase and the electrolyte within the pore space. Two models were used for the determination: an existing, computationally highly efficient analytical model developed in our group by Oehler et al. [15], and a numerical 3D model that was further developed in this work to simulate heterogeneous electrode microstructures, taken into account PSD, aspect ratios, and particle shape, among other factors.

The analytical model was used for the variation studies in order to take into account the broad spectrum of materials and design variations. Starting from a base configuration, the volume fractions of the AM phase, the composition of the BCA phase, the porosity, and the pure material data were varied. The variation was carried out with the aim of increasing or decreasing the effective thermal conductivity of the electrode in order to identify the extreme values in our permissible variation range. In addition to this sequential variation, the individual influence of the parameters was also investigated on the base configuration and the single-parameter influences were presented in scatter diagrams. In addition to the effective thermal conductivity, this variation was also carried out for the calculation of the effective density and specific heat capacity. The results of these variation studies are summarized in Fig. 8 or presented in scatter diagrams in supplementary section S5 and can serve as a database and guidance for thermal simulations, investigations, or designs, as only limited data is currently available.

The numerical model was used in order to assess the influence of the aspect ratio and particle shape on the effective thermal conductivity of

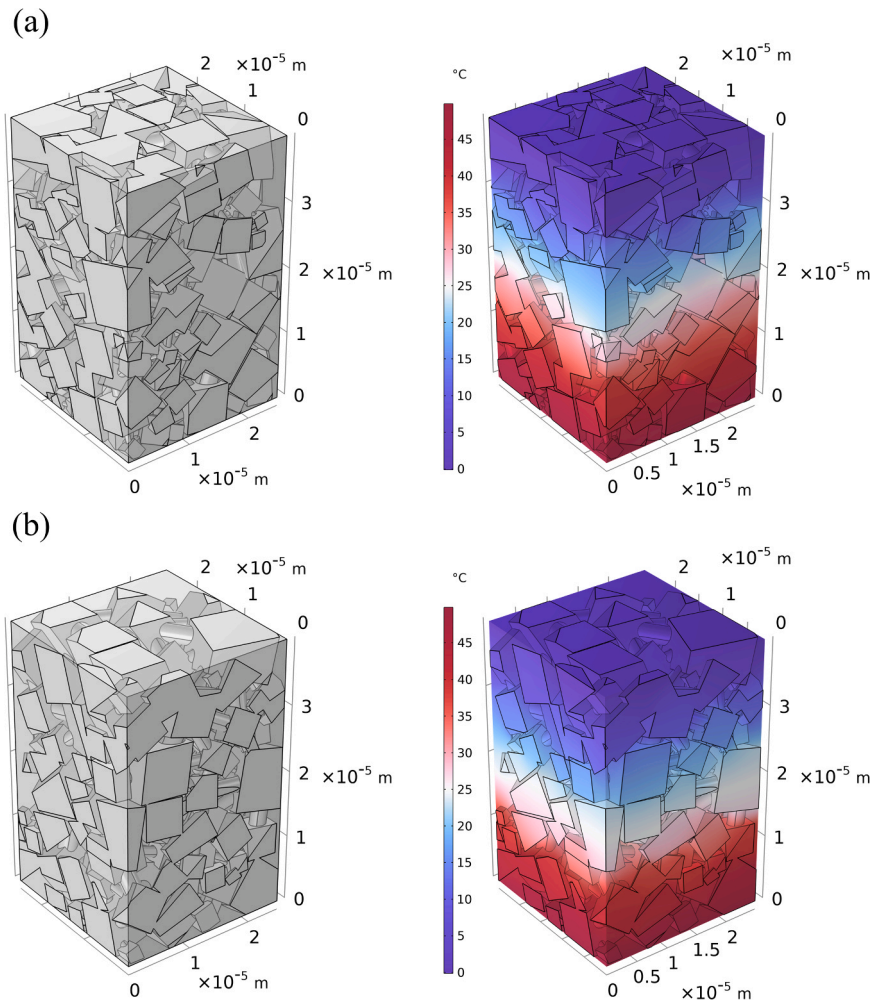

Fig. 11. Microstructure replication of generic Prussian blue electrodes with cube-shaped active material particles and polydisperse particle size distribution for two stochastically generated structures (a) and (b) with identical structural parameter specifications.

the electrodes and verify the analytical model. An NMC configuration was selected as the first case, in which the assumption of spherical active material particles is justified. The comparison of the numerically determined effective thermal conductivity shows very small deviations from the value determined with the analytical model and, consequently, very good agreement. In the case of ellipsoidal active material particles, such as those found in graphite electrodes, there are comparatively larger deviations for the determined effective thermal conductivity of the two models. If the underlying aspect ratio of the particles in the direction of the heat transport path is considered for the determination of the analytical model, the results also show very good agreement. Only the influence of the particle shape when changing from spherical to cubic active material particles, as is the case for Prussian blue, for example, currently shows potential for improvement in calculations using the analytical model.

In addition to further developing the analytical model to better replicate more complex active material shape, validating the studies using experimentally characterized electrodes is an essential next step. By specifically replicating the microstructures of electrodes with known composition ratios and electrode components used, it is possible to further develop the microstructure replication. In addition to replicating the volume proportions of the microstructure as accurately as possible, the focus here is also on accurately reproducing the PSD and BCA distribution as well as the active material particle shape. This enables, possibly supported by cross-section images, more precise knowledge about heat transport through the complex and very heterogeneous microstructure of a battery electrode and which parameters are to be considered particularly sensitive and which can be homogenized and simplified.

CRediT authorship contribution statement

Philipp Seegert: Writing – review & editing, Supervision, Software, Resources, Project administration, Methodology, Funding acquisition, Conceptualization. **Thomas Wetzel:** Writing – review & editing, Supervision, Resources, Project administration, Funding acquisition. **Leonie Pfeifer:** Writing – review & editing, Methodology, Conceptualization. **Raphael Mühlpfort:** Writing – review & editing, Writing – original draft, Visualization, Validation, Software, Project administration, Methodology, Investigation, Formal analysis, Data curation, Conceptualization.

Declaration of Competing Interest

The authors declare that they have no known competing financial interests or personal relationships that could have appeared to influence the work reported in this paper.

Acknowledgements

The authors would like to thank the Friedrich and Elisabeth Boysen Foundation for Research and Innovation for its financial support of this

project.

Appendix A. Supporting information

Supplementary data associated with this article can be found in the online version at doi:10.1016/j.fub.2026.100181.

Data availability

Data will be made available on request.

References

[1] W. Zhang, X. Fang, C. Sun, J. Environ. Manag. 341 (118019) (2023) 11, https://doi.org/10.1016/j.jenvman.2023.118019.
[2] T. Sutikno, W. Arsadiando, H.S. Purnama, Clean. Energy 9 (6) (2025) 293–322, https://doi.org/10.1093/ce/zkaf048.
[3] A. König, L. Nicoletti, D. Schröder, S. Wolff, A. Waclaw, M. Lienkamp, World Electr. Veh. J. 12 (1) (2021) 21, https://doi.org/10.3390/wevj12010021.
[4] S. Ma, M. Jiang, P. Tao, C. Song, J. Wu, J. Wang, et al., Prog. Nat. Sci. -Mater. 28 (6) (2018) 653–666, https://doi.org/10.1016/j.pnsc.2018.11.002.
[5] A.K. Koech, G. Mwandila, F. Mulolani, P. Mwaanga, S Afr. J. Chem. Eng. 50 (2024) 321–339, https://doi.org/10.1016/j.sajce.2024.09.008.
[6] S. Tan, H. Yang, Z. Zhang, X. Xu, Y. Xu, J. Zhou, et al., Molecules 28 (7) (2023) 3134, https://doi.org/10.3390/molecules28073134.
[7] D. Droese, P.M. Luc, M. Otto, A. Schlösser, D. Evans, J. Kowal, Batteries 11 (11) (2025 Nov 14) 420, https://doi.org/10.3390/batteries11110420.
[8] M. Steinhardt, J.V. Barreras, H. Ruan, B. Wu, G.J. Offer, A. Jossen, J. Power Sources 522 (2022) 230829, https://doi.org/10.1016/j.jpowsour.2021.230829.
[9] L. Spitthoff, M.S. Wahl, P.J.S. Vie, O.S. Burheim, J. Power Sources 577 (233149) (2023) 13, https://doi.org/10.1016/j.jpowsour.2023.233149.
[10] NEI Corporation [Shop] [Internet]. NEI Corporation. Available from: ⟨https://www.neicorporation.com⟩.
[11] MTI Corporation [Shop] [Internet]. MTI Corporation. Available from: ⟨https://mtixtl.com/en-euea⟩.
[12] A. Marconnet, S. Herberger, S. Paarmann, P. Seegert, T. Wetzel, J. Power Sources 603 (2024) 234367, https://doi.org/10.1016/j.jpowsour.2024.234367.
[13] L. Pfeifer, S. Herberger, T. Wetzel, P. Seegert, J. Power Sources 672 (239620) (2026) 12, https://doi.org/10.1016/j.jpowsour.2026.239620.
[14] D. Oehler, Bestimmung der thermischen Transporteigenschaften poröser Elektroden von Lithium-Ionen Batterien [Dissertation] [Internet], Karlsruher Institut für Technologie, Karlsruhe, 2021, https://doi.org/10.5445/KSP/1000136047.
[15] D. Oehler, P. Seegert, T. Wetzel, Energy Tech. 9 (200574) (2021) 16, https://doi.org/10.1002/ente.202000574.
[16] American Elements [Shop] [Internet]. [cited 2025 Sep 26]. Graphite, Natural Amorphous. Available from: ⟨https://americanelements.com/graphite-natural-amorphous-7782-42-5⟩.
[17] M. Zheng, Y. Liu, Z. Ma, Y. Li, D. Li, Z. Lu, et al., Energy Rep. 9 (2023) 350–361, https://doi.org/10.1016/j.egyr.2022.11.187.
[18] M. Mayur, M.C. Yagci, S. Carelli, P. Margulies, D. Velten, W.G. Bessler, Phys. Chem. Chem. Phys. 21 (23672) (2019) 23672–23684, https://doi.org/10.1039/C9CP04262H.
[19] D.R. Baker, M.W. Verbrugge, J. Electrochem Soc. 146 (7) (1999) 2413–2424, https://doi.org/10.1149/1.1391950.
[20] Sigma Aldrich [Shop] [Internet]. [cited 2025 Sep 26]. Graphite. Available from: ⟨https://www.sigmaaldrich.com/DE/en/product/aldrich/282863⟩.
[21] X. Dou, I. Hasa, D. Saurel, C. Vaalma, L. Wu, D. Buchholz, et al., Mater. Today 23 (2019) 87–104, https://doi.org/10.1016/j.mattod.2018.12.040.
[22] Data retrieved from the Materials Project for LiC6 (mp-1001581) from database version v2025.09.25. [Internet]. [cited 2025 Sep 26]. Available from: ⟨https://next-gen.materialsproject.org/materials/mp-1001581?_sort_fields=density&chemsys=Li-C⟩ doi:10.17188/1273021.
[23] Villars P., Cenzual K., editors. LiC6 Crystal Structure: Datasheet from "PAULING FILE Multinaries Edition – 2022" in SpringerMaterials (⟨https://materials.springer.com/isp/crystallographic/docs/sd_0377652⟩) [Internet]. Springer-Verlag Berlin Heidelberg & Material Phases Data System (MPDS), Switzerland & National Institute for Materials Science (NIMS), Japan; [cited 2025 Sep 26]. Available from: ⟨https://materials.springer.com/isp/crystallographic/docs/sd_0377652⟩.
[24] Data retrieved from the Materials Project for LiC12 (mp-1232339) from database version v2025.09.25. [Internet]. [cited 2025 Sep 26]. Available from: ⟨https://next-gen.materialsproject.org/materials/mp-1232339?_sort_fields=density&chemsys=Li-C⟩.
[25] Data retrieved from the Materials Project for LiC12 (mp-1021323) from database version v2025.09.25. [Internet]. [cited 2025 Sep 26]. Available from: ⟨https://next-gen.materialsproject.org/materials/mp-1021323?_sort_fields=density&chemsys=Li-C⟩ doi:10.17188/1351519.
[26] Villars P., Cenzual K., editors. LiC12 Crystal Structure: Datasheet from "PAULING FILE Multinaries Edition – 2022" in SpringerMaterials (⟨https://materials.springer.com/isp/crystallographic/docs/sd_1142469⟩) [Internet]. Springer-Verlag Berlin Heidelberg & Material Phases Data System (MPDS), Switzerland & National Institute for Materials Science (NIMS), Japan; [cited 2025 Sep 26]. Available from: ⟨https://materials.springer.com/isp/crystallographic/docs/sd_1142469⟩.
[27] Villars P., Cenzual K., editors. LiC24 in anode of Li-ion cell, charged to 4.45 V ((C) gra) Crystal Structure: Datasheet from "PAULING FILE Multinaries Edition – 2022" in SpringerMaterials (⟨https://materials.springer.com/isp/crystallographic/docs/sd_1607536⟩) [Internet]. Springer-Verlag Berlin Heidelberg & Material Phases Data System (MPDS), Switzerland & National Institute for Materials Science (NIMS), Japan; [cited 2025 Sep 26]. Available from: ⟨https://materials.springer.com/isp/crystallographic/docs/sd_1607536⟩.
[28] R.E. Gerver, J.P. Meyers, J. Electrochem Soc. 158 (7) (2011) A835–A836, https://doi.org/10.1149/1.3591799.
[29] A. Smontara, K. Biljaković, D. Starešinić, D. Pajić, M.E. Kozlov, M. Hirabayashi, et al., e. Phys. B Condens Matter 219 (220) (1996) 160–162, https://doi.org/10.1016/0921-4526(95)00682-6.
[30] X. Chen, C. Liu, Y. Fang, X. Ai, F. Zhong, H. Yang, et al., Carbon Energy 4 (6) (2022) 1133–1150, https://doi.org/10.1002/cey2.196.
[31] M. Kano, M. Momota, T. Okabe, K. Saito, Thermochim. Acta 292 (1997) 175–177, https://doi.org/10.1016/S0040-6031(96)03110-3.
[32] E.J. Cheng, K. Hong, N.J. Taylor, H. Choe, J. Wolfenstine, J. Sakamoto, J. Eur. Ceram. Soc. 37 (9) (2017) 3213–3217, https://doi.org/10.1016/j.jeurceramsoc.2017.03.048.
[33] H. Yang, C.N. Savory, B.J. Morgan, D.O. Scanlon, J.M. Skelton, A. Walsh, Chem. Mater. 32 (17) (2020) 7542–7550, https://doi.org/10.1021/acs.chemmater.0c02908.
[34] J. Cho, M.D. Losego, H.G. Zhang, H. Kim, J. Zuo, I. Petrov, et al., Nat. Commun. 5 (4035) (2014) 6, https://doi.org/10.1038/ncomms5035.
[35] J. Akimoto, Y. Gotoh, Y. Oosawa, J. Solid State Chem. 141 (SC987966) (1998) 298–302, https://doi.org/10.1006/jssc.1998.7966.
[36] E.J. Cheng, N.J. Taylor, J. Wolfenstine, J. Sakamoto, J. Asian Ceram. Soc. 5 (2) (2017) 113–117, https://doi.org/10.1016/j.jascer.2017.03.001.
[37] P. Gotcu, H.J. Seifert, Phys. Chem. Chem. Phys. 18 (15) (2016) 10550–10562, https://doi.org/10.1039/C6CP00887A.
[38] Data retrieved from the Materials Project for LiCoO2 (mp-849273) from database version v2025.06.09. [Internet]. [cited 2025 Sep 23]. Available from: ⟨https://next-gen.materialsproject.org/materials/mp-849273?_sort_fields=-density&formula=LiCoO2⟩.
[39] Data retrieved from the Materials Project for LiCoO2 (mp-753473) from database version v2025.06.09. [Internet]. [cited 2025 Sep 23]. Available from: ⟨https://next-gen.materialsproject.org/materials/mp-753473?_sort_fields=density&formula=LiCoO2⟩.
[40] Villars P., Cenzual K., editors. LiCoO2 Crystal Structure: Datasheet from "PAULING FILE Multinaries Edition – 2022" in SpringerMaterials (⟨https://materials.springer.com/isp/crystallographic/docs/sd_0554601⟩) [Internet]. Springer-Verlag Berlin Heidelberg & Material Phases Data System (MPDS), Switzerland & National Institute for Materials Science (NIMS), Japan; [cited 2025 Sep 23]. Available from: ⟨https://materials.springer.com/isp/crystallographic/docs/sd_0554601⟩.
[41] Sigma Aldrich [Shop] [Internet]. 442704 Lithium cobalt oxide. Available from: ⟨https://www.sigmaaldrich.com/DE/en/product/aldrich/442704⟩.
[42] P. Gotcu-Freis, D.M. Cupid, M. Rohde, H.J. Seifert, J. Chem. Thermodyn. 84 (2015) 118–127, https://doi.org/10.1016/j.jct.2014.12.007.
[43] Data retrieved from the Materials Project for LiFePO4 (mp-772093) from database version v2025.06.09. [Internet]. [cited 2025 Sep 19]. Available from: ⟨https://next-gen.materialsproject.org/materials/mp-772093?_sort_fields=-density&formula=LiFePO4#literature_references⟩.
[44] Data retrieved from the Materials Project for LiFePO4 (mp-772138) from database version v2025.06.09. [Internet]. [cited 2025 Sep 20]. Available from: ⟨https://next-gen.materialsproject.org/materials/mp-772138?_skip=60&_sort_fields=-density&formula=LiFePO4⟩.
[45] Villars P., Cenzual K., editors. LiFePO4 (LiFe[PO4] rt) Crystal Structure: Datasheet from "PAULING FILE Multinaries Edition – 2022" in SpringerMaterials (⟨https://materials.springer.com/isp/crystallographic/docs/sd_1958842⟩) [Internet]. Springer-Verlag Berlin Heidelberg & Material Phases Data System (MPDS), Switzerland & National Institute for Materials Science (NIMS), Japan. Available from: ⟨https://materials.springer.com/isp/crystallographic/docs/sd_1958842⟩.
[46] Sigma Aldrich [Shop] [Internet]. 759546 Lithium iron phosphate. Available from: ⟨https://www.sigmaaldrich.com/DE/en/product/aldrich/759546⟩.
[47] American Elements [Shop] [Internet]. [cited 2025 Sep 20]. Lithium Foil. Available from: ⟨https://americanelements.com/lithium-foil-7439-93-2⟩.
[48] Technical data for Lithium [Internet]. [cited 2025 Sep 20]. Available from: ⟨https://periodictable.com/Elements/003/data.html⟩.
[49] Data retrieved from the Materials Project for Li (mp-604313) from database version v2025.06.09. [Internet]. 2017. Available from: ⟨https://next-gen.materialsproject.org/materials/mp-604313?_sort_fields=density&formula=Li⟩ doi:10.17188/1277380.
[50] Data retrieved from the Materials Project for Li (mp-10173) from database version v2025.06.09. [Internet]. 2020. Available from: ⟨https://next-gen.materialsproject.org/materials/mp-10173?_sort_fields=-density&formula=Li⟩ doi:10.17188/1186702.
[51] Villars P., Cenzual K., editors. LiMn1−xFexPO4, x= 0.5 (LiMn0.5Fe0.5[PO4]) Crystal Structure: Datasheet from "PAULING FILE Multinaries Edition – 2022" in SpringerMaterials (⟨https://materials.springer.com/isp/crystallographic/docs/sd_1031133⟩) [Internet]. Springer-Verlag Berlin Heidelberg & Material Phases Data System (MPDS), Switzerland & National Institute for Materials

Science (NIMS), Japan. Available from: ⟨https://materials.springer.com/isp/crystallographic/docs/sd_1031133⟩.
[52] Villars P., Cenzual K., editors. Li(Mn0.6Fe0.4)PO4 (LiMn0.5Fe0.5[PO4]) Crystal Structure: Datasheet from "PAULING FILE Multinaries Edition – 2022" in SpringerMaterials (⟨https://materials.springer.com/isp/crystallographic/docs/sd_1522470⟩) [Internet]. Springer-Verlag Berlin Heidelberg & Material Phases Data System (MPDS), Switzerland & National Institute for Materials Science (NIMS), Japan; [cited 2025 Sep 20]. Available from: ⟨https://materials.springer.com/isp/crystallographic/docs/sd_1522470⟩.
[53] Villars P., Cenzual K., editors. LiMn1−xFexPO4/C, x= 0.3 (LiMn0.7Fe0.3[PO4]) Crystal Structure: Datasheet from "PAULING FILE Multinaries Edition – 2022" in SpringerMaterials (⟨https://materials.springer.com/isp/crystallographic/docs/sd_1953940⟩) [Internet]. Springer-Verlag Berlin Heidelberg & Material Phases Data System (MPDS), Switzerland & National Institute for Materials Science (NIMS), Japan. Available from: ⟨https://materials.springer.com/isp/crystallographic/docs/sd_1953940⟩.
[54] Villars P., Cenzual K., editors. LiMn0.8Fe0.2PO4 (LiMn0.5Fe0.5[PO4]) Crystal Structure: Datasheet from "PAULING FILE Multinaries Edition – 2022" in SpringerMaterials (⟨https://materials.springer.com/isp/crystallographic/docs/sd_1049708⟩) [Internet]. Springer-Verlag Berlin Heidelberg & Material Phases Data System (MPDS), Switzerland & National Institute for Materials Science (NIMS), Japan. Available from: ⟨https://materials.springer.com/isp/crystallographic/docs/sd_1049708⟩.
[55] Villars P., Cenzual K., editors. LiFe1−xMnxPO4, x= 0.85 (LiMn0.5Fe0.5[PO4]) Crystal Structure: Datasheet from "PAULING FILE Multinaries Edition – 2022" in SpringerMaterials (⟨https://materials.springer.com/isp/crystallographic/docs/sd_1248932⟩) [Internet]. Springer-Verlag Berlin Heidelberg & Material Phases Data System (MPDS), Switzerland & National Institute for Materials Science (NIMS), Japan. Available from: ⟨https://materials.springer.com/isp/crystallographic/docs/sd_1248932⟩.
[56] Villars P., Cenzual K., editors. LiFe1−xMnxPO4, x= 0.90 (LiMn0.5Fe0.5[PO4]) Crystal Structure: Datasheet from "PAULING FILE Multinaries Edition – 2022" in SpringerMaterials (⟨https://materials.springer.com/isp/crystallographic/docs/sd_1248933⟩) [Internet]. Springer-Verlag Berlin Heidelberg & Material Phases Data System (MPDS), Switzerland & National Institute for Materials Science (NIMS), Japan. Available from: ⟨https://materials.springer.com/isp/crystallographic/docs/sd_1248933⟩.
[57] Data retrieved from the Materials Project for Li2Mn3NiO8 (mp-753229) from database version v2025.06.09. [Internet]. [cited 2025 Sep 22]. Available from: ⟨https://next-gen.materialsproject.org/materials/mp-753229?_sort_fields=density&formula=Li2Mn3NiO8⟩.
[58] Data retrieved from the Materials Project for Li2Mn3NiO8 (mp-771971) from database version v2025.06.09. [Internet]. [cited 2025 Sep 22]. Available from: ⟨https://next-gen.materialsproject.org/materials/mp-771971?_sort_fields=density&formula=Li2Mn3NiO8⟩.
[59] Villars P., Cenzual K., editors. LiNi0.5Mn1.5O4 (LiMn1.5Ni0.5O4 cub1) Crystal Structure: Datasheet from "PAULING FILE Multinaries Edition – 2022" in SpringerMaterials (⟨https://materials.springer.com/isp/crystallographic/docs/sd_0314662⟩) [Internet]. Springer-Verlag Berlin Heidelberg & Material Phases Data System (MPDS), Switzerland & National Institute for Materials Science (NIMS), Japan. Available from: ⟨https://materials.springer.com/isp/crystallographic/docs/sd_0314662⟩.
[60] Data retrieved from the Materials Project for LiMnO2 (mp-37620) from database version v2025.06.09. [Internet]. [cited 2025 Sep 22]. Available from: ⟨https://next-gen.materialsproject.org/materials/mp-37620?_sort_fields=-density&formula=LiMnO2⟩ doi:10.17188/1207387.
[61] Data retrieved from the Materials Project for LiMnO2 (mp-35929) from database version v2025.06.09. [Internet]. [cited 2025 Sep 22]. Available from: ⟨https://next-gen.materialsproject.org/materials/mp-35929?_sort_fields=density&formula=LiMnO2⟩ doi:10.17188/1207103.
[62] Villars P., Cenzual K., editors. LiMn2O4 Crystal Structure: Datasheet from "PAULING FILE Multinaries Edition – 2022" in SpringerMaterials (⟨https://materials.springer.com/isp/crystallographic/docs/sd_1004188⟩) [Internet]. Springer-Verlag Berlin Heidelberg & Material Phases Data System (MPDS), Switzerland & National Institute for Materials Science (NIMS), Japan. Available from: ⟨https://materials.springer.com/isp/crystallographic/docs/sd_1004188⟩.
[63] P. Huang, P. Ping, K. Li, H. Chen, Q. Wang, J. Wen, et al., Appl. Energy 183 (2016) 659–673, https://doi.org/10.1016/j.apenergy.2016.08.160.
[64] Data retrieved from the Materials Project for Li4Ti5O12 (mp-772925) from database version v2025.09.25. [Internet]. 2020 [cited 2025 Sep 26]. Available from: ⟨https://next-gen.materialsproject.org/materials/mp-772925?_sort_fields=density&formula=Li4Ti5O12⟩ doi:10.17188/1301539.
[65] Data retrieved from the Materials Project for Li4Ti5O12 (mp-685194) from database version v2025.09.25. [Internet]. 2020 [cited 2025 Sep 26]. Available from: ⟨https://next-gen.materialsproject.org/materials/mp-685194?_sort_fields=density&formula=Li4Ti5O12⟩ doi:10.17188/1284125.
[66] American Elements [Shop] [Internet]. [cited 2025 Sep 26]. Lithium Titanate, Spinel Nanoparticles / Nanopowder. Available from: ⟨https://americanelements.com/lithium-titanate-spinel-nanoparticles-nanopowder-12031-95-7⟩.
[67] Villars P., Cenzual K., editors. Li4Ti5O12 (Li1.33Ti1.67O4) Crystal Structure: Datasheet from "PAULING FILE Multinaries Edition – 2022" in SpringerMaterials (⟨https://materials.springer.com/isp/crystallographic/docs/sd_1942193⟩) [Internet]. Springer-Verlag Berlin Heidelberg & Material Phases Data System (MPDS), Switzerland & National Institute for Materials Science (NIMS), Japan; [cited 2025 Sep 26]. Available from: ⟨https://materials.springer.com/isp/crystallographic/docs/sd_1942193⟩.
[68] Villars P., Cenzual K., editors. Li4Ti5O12 (Li1.33Ti1.67O4, T = 1173 K) Crystal Structure: Datasheet from "PAULING FILE Multinaries Edition – 2022" in SpringerMaterials (⟨https://materials.springer.com/isp/crystallographic/docs/sd_1632094⟩) [Internet]. Springer-Verlag Berlin Heidelberg & Material Phases Data System (MPDS), Switzerland & National Institute for Materials Science (NIMS), Japan; [cited 2025 Sep 26]. Available from: ⟨https://materials.springer.com/isp/crystallographic/docs/sd_1632094⟩.
[69] American Elements [Shop] [Internet]. [cited 2025 Sep 26]. Lithium Titanate. Available from: ⟨https://americanelements.com/lithium-titanate-12031-82-2⟩.
[70] H. Kleykamp, J. Nucl. Mater. 295 (2001) 244–248, https://doi.org/10.1016/S0022-3115(01)00550-5.
[71] Technical data for Sodium [Internet]. [cited 2025 Sep 20]. Available from: ⟨https://periodictable.com/Elements/011/data.html⟩.
[72] Data retrieved from the Materials Project for Na (mp-999501) from database version v2025.06.09. [Internet]. 2020. Available from: ⟨https://next-gen.materialsproject.org/materials/mp-999501?_sort_fields=density&formula=Na⟩ doi:10.17188/1317595.
[73] Data retrieved from the Materials Project for Na (mp-10172) from database version v2025.06.09. [Internet]. 2020. Available from: ⟨https://next-gen.materialsproject.org/materials/mp-10172?_sort_fields=-density&formula=Na⟩ doi:10.17188/1186701.
[74] G. Liu, L. Zhang, World Electr. Veh. J. 12 (4) (2021) 250, https://doi.org/10.3390/wevj12040250.
[75] American Elements [Shop] [Internet]. [cited 2025 Sep 23]. Lithium Nickel Cobalt Aluminum Oxide. Available from: ⟨https://americanelements.com/lithium-nickel-cobalt-aluminum-oxide-193214-24-3⟩.
[76] Villars P., Cenzual K., editors. LiNi0.3Al0.2Co0.5O2 (LiCo0.15Ni0.7Al0.15O2) Crystal Structure: Datasheet from "PAULING FILE Multinaries Edition – 2022" in SpringerMaterials (⟨https://materials.springer.com/isp/crystallographic/docs/sd_1023507⟩) [Internet]. Springer-Verlag Berlin Heidelberg & Material Phases Data System (MPDS), Switzerland & National Institute for Materials Science (NIMS), Japan. Available from: ⟨https://materials.springer.com/isp/crystallographic/docs/sd_1023507⟩.
[77] Villars P., Cenzual K., editors. LiNi0.80Co0.15Al0.05O2 (LiCo0.15Ni0.7Al0.15O2) Crystal Structure: Datasheet from "PAULING FILE Multinaries Edition – 2022" in SpringerMaterials (⟨https://materials.springer.com/isp/crystallographic/docs/sd_1044193⟩) [Internet]. Springer-Verlag Berlin Heidelberg & Material Phases Data System (MPDS), Switzerland & National Institute for Materials Science (NIMS), Japan. Available from: ⟨https://materials.springer.com/isp/crystallographic/docs/sd_1044193⟩.
[78] Sigma Aldrich [Shop] [Internet]. 760994 Lithium nickel cobalt aluminium oxide. Available from: ⟨https://www.sigmaaldrich.com/DE/en/product/aldrich/760994⟩.
[79] Data retrieved from the Materials Project for NaCoPO4 (mp-562796) from database version v2025.09.25. [Internet]. [cited 2025 Sep 26]. Available from: ⟨https://next-gen.materialsproject.org/materials/mp-562796?_sort_fields=density&formula=NaCoPO4⟩.
[80] Data retrieved from the Materials Project for NaCoPO4 (mp-18245) from database version v2025.09.25. [Internet]. [cited 2025 Sep 26]. Available from: ⟨https://next-gen.materialsproject.org/materials/mp-18245?_sort_fields=density&formula=NaCoPO4⟩.
[81] Villars P., Cenzual K., editors. β-NaCoPO4 (NaCo[PO4] hex) Crystal Structure: Datasheet from "PAULING FILE Multinaries Edition – 2022" in SpringerMaterials (⟨https://materials.springer.com/isp/crystallographic/docs/sd_1051984⟩) [Internet]. Springer-Verlag Berlin Heidelberg & Material Phases Data System (MPDS), Switzerland & National Institute for Materials Science (NIMS), Japan; [cited 2025 Sep 26]. Available from: ⟨https://materials.springer.com/isp/crystallographic/docs/sd_1051984⟩.
[82] Villars P., Cenzual K., editors. α-NaCoPO4 (NaCo[PO4] rt) Crystal Structure: Datasheet from "PAULING FILE Multinaries Edition – 2022" in SpringerMaterials (⟨https://materials.springer.com/isp/crystallographic/docs/sd_1050040⟩) [Internet]. Springer-Verlag Berlin Heidelberg & Material Phases Data System (MPDS), Switzerland & National Institute for Materials Science (NIMS), Japan; [cited 2025 Sep 26]. Available from: ⟨https://materials.springer.com/isp/crystallographic/docs/sd_1050040⟩.
[83] Villars P., Cenzual K., editors. O3-NaFe0.3Ni0.35Mn0.35O2 (NaMn0.3Fe0.4Ni0.3O2) Crystal Structure: Datasheet from "PAULING FILE Multinaries Edition – 2022" in SpringerMaterials (⟨https://materials.springer.com/isp/crystallographic/docs/sd_1149570⟩) [Internet]. Springer-Verlag Berlin Heidelberg & Material Phases Data System (MPDS), Switzerland & National Institute for Materials Science (NIMS), Japan; [cited 2025 Sep 26]. Available from: ⟨https://materials.springer.com/isp/crystallographic/docs/sd_1149570⟩.
[84] Villars P., Cenzual K., editors. P2-Na2/3[Ni1/3−xMn2/3−yFex+y]O2, x= y= 1/36 (Na0.5Mn0.63Fe0.13Ni0.23O2) Crystal Structure: Datasheet from "PAULING FILE Multinaries Edition – 2022" in SpringerMaterials (⟨https://materials.springer.com/isp/crystallographic/docs/sd_1224283⟩) [Internet]. Springer-Verlag Berlin Heidelberg & Material Phases Data System (MPDS), Switzerland & National Institute for Materials Science (NIMS), Japan; [cited 2025 Sep 26]. Available from: ⟨https://materials.springer.com/isp/crystallographic/docs/sd_1224283⟩.
[85] Data retrieved from the Materials Project for NaFePO4 (mp-1192859) from database version v2025.09.25. [Internet]. [cited 2025 Sep 26]. Available from: ⟨https://next-gen.materialsproject.org/materials/mp-1192859?_sort_fields=density&formula=NaFePO4⟩.
[86] Data retrieved from the Materials Project for NaFePO4 (mp-19226) from database version v2025.09.25. [Internet]. [cited 2025 Sep 26]. Available from: ⟨https://n

ext-gen.materialsproject.org/materials/mp-19226?_sort_fields=density&formula=NaFePO4⟩ doi:10.17188/1194087.
[87] Villars P., Cenzual K., editors. NaFePO4 (NaFe[PO4]) Crystal Structure: Datasheet from "PAULING FILE Multinaries Edition – 2022" in SpringerMaterials (⟨https://materials.springer.com/isp/crystallographic/docs/sd_1012977⟩) [Internet]. Springer-Verlag Berlin Heidelberg & Material Phases Data System (MPDS), Switzerland & National Institute for Materials Science (NIMS), Japan; [cited 2025 Sep 26]. Available from: ⟨https://materials.springer.com/isp/crystallographic/docs/sd_1012977⟩.
[88] Villars P., Cenzual K., editors. NaFePO4 (NaFe[PO4]) Crystal Structure: Datasheet from "PAULING FILE Multinaries Edition – 2022" in SpringerMaterials (⟨https://materials.springer.com/isp/crystallographic/docs/sd_1632128⟩) [Internet]. Springer-Verlag Berlin Heidelberg & Material Phases Data System (MPDS), Switzerland & National Institute for Materials Science (NIMS), Japan; [cited 2025 Sep 26]. Available from: ⟨https://materials.springer.com/isp/crystallographic/docs/sd_1632128⟩.
[89] Villars P., Cenzual K., editors. LiNi1/3Co1/3Mn1/3O2 (LiMn0.33Co0.33Ni0.33O2) Crystal Structure: Datasheet from "PAULING FILE Multinaries Edition – 2022" in SpringerMaterials (⟨https://materials.springer.com/isp/crystallographic/docs/sd_1022154⟩) [Internet]. Springer-Verlag Berlin Heidelberg & Material Phases Data System (MPDS), Switzerland & National Institute for Materials Science (NIMS), Japan. Available from: ⟨https://materials.springer.com/isp/crystallographic/docs/sd_1022154⟩.
[90] H. Sun, K. Zhao, J. Phys. Chem. C. 121 (2017) 6002–6010, https://doi.org/10.1021/acs.jpcc.7b00810.
[91] R. Chowdhury, Y. Zhao, Y. Xia, M. Ouyang, N. Brandon, A. Banerjee, Sustain Energy Fuels 5 (2021) 5193–5204, https://doi.org/10.1039/D1SE01077H.
[92] Villars P., Cenzual K., editors. Li(Ni0.5Co0.2Mn0.3)O2 (LiMn0.33Co0.33Ni0.33O2) Crystal Structure: Datasheet from "PAULING FILE Multinaries Edition – 2022" in SpringerMaterials (⟨https://materials.springer.com/isp/crystallographic/docs/sd_1047369⟩) [Internet]. Springer-Verlag Berlin Heidelberg & Material Phases Data System (MPDS), Switzerland & National Institute for Materials Science (NIMS), Japan; [cited 2025 Sep 22]. Available from: ⟨https://materials.springer.com/isp/crystallographic/docs/sd_1047369⟩.
[93] Villars P., Cenzual K., editors. LiNi0.6Co0.2Mn0.2O2 (LiMn0.33Co0.33Ni0.33O2) Crystal Structure: Datasheet from "PAULING FILE Multinaries Edition – 2022" in SpringerMaterials (⟨https://materials.springer.com/isp/crystallographic/docs/sd_1050219⟩) [Internet]. Springer-Verlag Berlin Heidelberg & Material Phases Data System (MPDS), Switzerland & National Institute for Materials Science (NIMS), Japan. Available from: ⟨https://materials.springer.com/isp/crystallographic/docs/sd_1050219⟩.
[94] Villars P., Cenzual K., editors. LiNi0.8Co0.1Mn0.1O2 (LiMn0.33Co0.33Ni0.33O2) Crystal Structure: Datasheet from "PAULING FILE Multinaries Edition – 2022" in SpringerMaterials (⟨https://materials.springer.com/isp/crystallographic/docs/sd_1042334⟩) [Internet]. Springer-Verlag Berlin Heidelberg & Material Phases Data System (MPDS), Switzerland & National Institute for Materials Science (NIMS), Japan. Available from: ⟨https://materials.springer.com/isp/crystallographic/docs/sd_1042334⟩.
[95] Villars P., Cenzual K., editors. LiNi0.8Co0.1Mn0.1O2 (LiMn0.33Co0.33Ni0.33O2) Crystal Structure: Datasheet from "PAULING FILE Multinaries Edition – 2022" in SpringerMaterials (⟨https://materials.springer.com/isp/crystallographic/docs/sd_1046215⟩) [Internet]. Springer-Verlag Berlin Heidelberg & Material Phases Data System (MPDS), Switzerland & National Institute for Materials Science (NIMS), Japan. Available from: ⟨https://materials.springer.com/isp/crystallographic/docs/sd_1046215⟩.
[96] Villars P., Cenzual K., editors. Li1.2Mn0.54Ni0.13Co0.13O2 (LiMn0.33Co0.33Ni0.33O2) Crystal Structure: Datasheet from "PAULING FILE Multinaries Edition – 2022" in SpringerMaterials (⟨https://materials.springer.com/isp/crystallographic/docs/sd_1046376⟩) [Internet]. Springer-Verlag Berlin Heidelberg & Material Phases Data System (MPDS), Switzerland & National Institute for Materials Science (NIMS), Japan; [cited 2025 Sep 22]. Available from: ⟨https://materials.springer.com/isp/crystallographic/docs/sd_1046376⟩.
[97] I.U. Mohsin, C. Ziebert, M. Rohde, H.J. Seifert, Batteries 7 (2021) 16, https://doi.org/10.3390/batteries7010016.
[98] Villars P., Cenzual K., editors. Na0.44MnO2 (Na3.6Mn9O18 ht) Crystal Structure: Datasheet from "PAULING FILE Multinaries Edition – 2022" in SpringerMaterials (⟨https://materials.springer.com/isp/crystallographic/docs/sd_1343662⟩) [Internet]. Springer-Verlag Berlin Heidelberg & Material Phases Data System (MPDS), Switzerland & National Institute for Materials Science (NIMS), Japan; [cited 2025 Sep 26]. Available from: ⟨https://materials.springer.com/isp/crystallographic/docs/sd_1343662⟩.
[99] Villars P., Cenzual K., editors. NaxCoO2, x= 0.68 (Na0.7CoO2 rt) Crystal Structure: Datasheet from "PAULING FILE Multinaries Edition – 2022" in SpringerMaterials (⟨https://materials.springer.com/isp/crystallographic/docs/sd_1628718⟩) [Internet]. Springer-Verlag Berlin Heidelberg & Material Phases Data System (MPDS), Switzerland & National Institute for Materials Science (NIMS), Japan; [cited 2025 Sep 26]. Available from: ⟨https://materials.springer.com/isp/crystallographic/docs/sd_1628718⟩.
[100] Data retrieved from the Materials Project for NaMnO2 (mp-1016119) from database version v2025.09.25. [Internet]. [cited 2025 Sep 26]. Available from: ⟨https://next-gen.materialsproject.org/materials/mp-1016119?_sort_fields=density&formula=NaMnO2⟩.
[101] Data retrieved from the Materials Project for NaMnO2 (mp-18957) from database version v2025.09.25. [Internet]. [cited 2025 Sep 26]. Available from: ⟨https://next-gen.materialsproject.org/materials/mp-18957?_sort_fields=density&formula=NaMnO2⟩ doi:10.17188/1193732.
[102] Villars P., Cenzual K., editors. NaMnO2 Crystal Structure: Datasheet from "PAULING FILE Multinaries Edition – 2022" in SpringerMaterials (⟨https://materials.springer.com/isp/crystallographic/docs/sd_1213513⟩) [Internet]. Springer-Verlag Berlin Heidelberg & Material Phases Data System (MPDS), Switzerland & National Institute for Materials Science (NIMS), Japan; [cited 2025 Sep 26]. Available from: ⟨https://materials.springer.com/isp/crystallographic/docs/sd_1213513⟩.
[103] Data retrieved from the Materials Project for NaMnPO4 (mp-775855) from database version v2025.09.25. [Internet]. [cited 2025 Sep 26]. Available from: ⟨https://next-gen.materialsproject.org/materials/mp-775855?_sort_fields=density&formula=NaMnPO4⟩.
[104] Data retrieved from the Materials Project for NaMnPO4 (mp-17967) from database version v2025.09.25. [Internet]. [cited 2025 Sep 26]. Available from: ⟨https://next-gen.materialsproject.org/materials/mp-17967?_sort_fields=density&formula=NaMnPO4⟩.
[105] Villars P., Cenzual K., editors. NaMnPO4 ht polymorph (NaMn[PO4] ht) Crystal Structure: Datasheet from "PAULING FILE Multinaries Edition – 2022" in SpringerMaterials (⟨https://materials.springer.com/isp/crystallographic/docs/sd_1538619⟩) [Internet]. Springer-Verlag Berlin Heidelberg & Material Phases Data System (MPDS), Switzerland & National Institute for Materials Science (NIMS), Japan; [cited 2025 Sep 26]. Available from: ⟨https://materials.springer.com/isp/crystallographic/docs/sd_1538619⟩.
[106] Villars P., Cenzual K., editors. NaMnPO4 (NaMn[PO4] rt) Crystal Structure: Datasheet from "PAULING FILE Multinaries Edition – 2022" in SpringerMaterials (⟨https://materials.springer.com/isp/crystallographic/docs/sd_1632129⟩) [Internet]. Springer-Verlag Berlin Heidelberg & Material Phases Data System (MPDS), Switzerland & National Institute for Materials Science (NIMS), Japan; [cited 2025 Sep 26]. Available from: ⟨https://materials.springer.com/isp/crystallographic/docs/sd_1632129⟩.
[107] Villars P., Cenzual K. P3-Na2/3[Ni1/3Mn2/3]O2 (Na0.7Mn0.5Ni0.5O2 rhom) Crystal Structure: Datasheet from "PAULING FILE Multinaries Edition – 2022" in SpringerMaterials (⟨https://materials.springer.com/isp/crystallographic/docs/sd_1004717⟩) [Internet]. Springer-Verlag Berlin Heidelberg & Material Phases Data System (MPDS), Switzerland & National Institute for Materials Science (NIMS), Japan; [cited 2025 Dec 26]. Available from: ⟨https://materials.springer.com/isp/crystallographic/docs/sd_1004717⟩.
[108] Villars P., Cenzual K. O3-Na[Ni1/2Mn1/2]O2 (NaMn0.5Ni0.5O2) Crystal Structure: Datasheet from "PAULING FILE Multinaries Edition – 2022" in SpringerMaterials (⟨https://materials.springer.com/isp/crystallographic/docs/sd_1004720⟩) [Internet]. Springer-Verlag Berlin Heidelberg & Material Phases Data System (MPDS), Switzerland & National Institute for Materials Science (NIMS), Japan; [cited 2025 Dec 26]. Available from: ⟨https://materials.springer.com/isp/crystallographic/docs/sd_1004720⟩.
[109] Villars P., Cenzual K. Na0.44Mn0.6Ni0.4O2 (Na0.7Mn0.5Ni0.5O2 hex) Crystal Structure: Datasheet from "PAULING FILE Multinaries Edition – 2022" in SpringerMaterials (⟨https://materials.springer.com/isp/crystallographic/docs/sd_1049296⟩) [Internet]. Springer-Verlag Berlin Heidelberg & Material Phases Data System (MPDS), Switzerland & National Institute for Materials Science (NIMS), Japan; [cited 2025 Dec 26]. Available from: ⟨https://materials.springer.com/isp/crystallographic/docs/sd_1049296⟩.
[110] Data retrieved from the Materials Project for NaNiPO4 (mp-776388) from database version v2025.09.25. [Internet]. [cited 2025 Dec 28]. Available from: ⟨https://next-gen.materialsproject.org/materials/mp-776388?_sort_fields=density&formula=NaNiPO4⟩.
[111] Data retrieved from the Materials Project for NaNiPO4 (mp-761066) from database version v2025.09.25. [Internet]. [cited 2025 Dec 28]. Available from: ⟨https://next-gen.materialsproject.org/materials/mp-761066?_sort_fields=density&formula=NaNiPO4⟩.
[112] Villars P., Cenzual K. NaNiPO4 (NaNi[PO4]) Crystal Structure: Datasheet from "PAULING FILE Multinaries Edition – 2022" in SpringerMaterials (⟨https://materials.springer.com/isp/crystallographic/docs/sd_1143540⟩) [Internet]. Springer-Verlag Berlin Heidelberg & Material Phases Data System (MPDS), Switzerland & National Institute for Materials Science (NIMS), Japan; [cited 2025 Dec 28]. Available from: ⟨https://materials.springer.com/isp/crystallographic/docs/sd_1143540⟩.
[113] Data retrieved from the Materials Project for Na2Ti3O7 (mp-3488) from database version v2025.09.25. [Internet]. 2020 [cited 2025 Dec 28]. Available from: ⟨https://next-gen.materialsproject.org/materials/mp-3488?_sort_fields=density&formula=Na2Ti3O7⟩ doi:10.17188/1206899.
[114] Villars P., Cenzual K. Na2Ti3O7 Crystal Structure: Datasheet from "PAULING FILE Multinaries Edition – 2022" in SpringerMaterials (⟨https://materials.springer.com/isp/crystallographic/docs/sd_0310586⟩) [Internet]. Springer-Verlag Berlin Heidelberg & Material Phases Data System (MPDS), Switzerland & National Institute for Materials Science (NIMS), Japan; [cited 2025 Dec 28]. Available from: ⟨https://materials.springer.com/isp/crystallographic/docs/sd_0310586⟩.
[115] Data retrieved from the Materials Project for Na4Ti5O12 (mp-760184) from database version v2025.09.25. [Internet]. 2020 [cited 2025 Dec 28]. Available from: ⟨https://next-gen.materialsproject.org/materials/mp-760184?_sort_fields=density&formula=Na4Ti5O12⟩ doi:10.17188/1291589.
[116] Data retrieved from the Materials Project for Na4Ti5O12 (mp-555678) from database version v2025.09.25. [Internet]. 2020 [cited 2025 Dec 28]. Available from: ⟨https://next-gen.materialsproject.org/materials/mp-555678?_sort_fields=density&formula=Na4Ti5O12⟩ doi:10.17188/1268932.
[117] Villars P., Cenzual K. M-Na4.6Ti5O12 (Na4Ti5O12 ht) Crystal Structure: Datasheet from "PAULING FILE Multinaries Edition – 2022" in SpringerMaterials (⟨https://materials.springer.com/isp/crystallographic/docs/sd_1141966⟩)

[Internet]. Springer-Verlag Berlin Heidelberg & Material Phases Data System (MPDS), Switzerland & National Institute for Materials Science (NIMS), Japan; [cited 2025 Dec 28]. Available from: ⟨https://materials.springer.com/isp/crystallographic/docs/sd_1141966⟩.
[118] Villars P., Cenzual K. M-Na4Ti5O12 (Na4Ti5O12 ht) Crystal Structure: Datasheet from "PAULING FILE Multinaries Edition – 2022" in SpringerMaterials (⟨https://materials.springer.com/isp/crystallographic/docs/sd_1141961⟩) [Internet]. Springer-Verlag Berlin Heidelberg & Material Phases Data System (MPDS), Switzerland & National Institute for Materials Science (NIMS), Japan; [cited 2025 Dec 28]. Available from: ⟨https://materials.springer.com/isp/crystallographic/docs/sd_1141961⟩.
[119] Villars P., Cenzual K. Na4Ti5O12 Crystal Structure: Datasheet from "PAULING FILE Multinaries Edition – 2022" in SpringerMaterials (⟨https://materials.springer.com/isp/crystallographic/docs/sd_1129329⟩) [Internet]. Springer-Verlag Berlin Heidelberg & Material Phases Data System (MPDS), Switzerland & National Institute for Materials Science (NIMS), Japan; [cited 2025 Dec 28]. Available from: ⟨https://materials.springer.com/isp/crystallographic/docs/sd_1129329⟩.
[120] Data retrieved from the Materials Project for NaTi2(PO4)3 (mp-776599) from database version v2025.09.25. [Internet]. 2020 [cited 2025 Dec 28]. Available from: ⟨https://next-gen.materialsproject.org/materials/mp-776599?formula=NaTi2⟩(PO4)3 doi:10.17188/1304319.
[121] Data retrieved from the Materials Project for NaTi2(PO4)3 (mp-776567) from database version v2025.09.25. [Internet]. 2020 [cited 2025 Dec 28]. Available from: ⟨https://next-gen.materialsproject.org/materials/mp-776567?_sort_fields=density&formula=NaTi2%28PO4%293⟩ doi:10.17188/1304313.
[122] Villars P., Cenzual K. NaTi2(PO4)3 (NaTi2[PO4]3 rhom) Crystal Structure: Datasheet from "PAULING FILE Multinaries Edition – 2022" in SpringerMaterials (⟨https://materials.springer.com/isp/crystallographic/docs/sd_0543090⟩) [Internet]. Springer-Verlag Berlin Heidelberg & Material Phases Data System (MPDS), Switzerland & National Institute for Materials Science (NIMS), Japan; [cited 2025 Dec 28]. Available from: ⟨https://materials.springer.com/isp/crystallographic/docs/sd_0543090⟩.
[123] Villars P., Cenzual K. NaTi2(PO4)3 (NaTi2[PO4]3 rhom) Crystal Structure: Datasheet from "PAULING FILE Multinaries Edition – 2022" in SpringerMaterials (⟨https://materials.springer.com/isp/crystallographic/docs/sd_0313852⟩) [Internet]. Springer-Verlag Berlin Heidelberg & Material Phases Data System (MPDS), Switzerland & National Institute for Materials Science (NIMS), Japan; [cited 2025 Dec 28]. Available from: ⟨https://materials.springer.com/isp/crystallographic/docs/sd_0313852⟩.
[124] X. Jin, X. Ding, F. Zhan, Q. Gao, R. Wang, X. Yang, et al., J. Phys. Chem. Lett. 13 (2022) 11160–11168, https://doi.org/10.1021/acs.jpclett.2c03061.
[125] Data retrieved from the Materials Project for NaVO3 (mp-1101657) from database version v2025.09.25. [Internet]. [cited 2025 Dec 28]. Available from: ⟨https://next-gen.materialsproject.org/materials/mp-1101657?_sort_fields=density&formula=NaVO3⟩.
[126] Data retrieved from the Materials Project for NaVO3 (mp-1099591) from database version v2025.09.25. [Internet]. [cited 2025 Dec 28]. Available from: ⟨https://next-gen.materialsproject.org/materials/mp-1099591?_sort_fields=density&formula=NaVO3⟩.
[127] Villars P., Cenzual K. NaVO3 Crystal Structure: Datasheet from "PAULING FILE Multinaries Edition – 2022" in SpringerMaterials (⟨https://materials.springer.com/isp/crystallographic/docs/sd_0551615⟩) [Internet]. Springer-Verlag Berlin Heidelberg & Material Phases Data System (MPDS), Switzerland & National Institute for Materials Science (NIMS), Japan; [cited 2025 Dec 28]. Available from: ⟨https://materials.springer.com/isp/crystallographic/docs/sd_0551615⟩.
[128] G. Pei, J. Xiang, X. Lv, G. Li, S. Wu, D. Zhong, et al., J. Alloy. Compd. 794 (2019) 465–472, https://doi.org/10.1016/j.jallcom.2019.04.186.
[129] Data retrieved from the Materials Project for Na3V2(PO4)3 (mp-761059) from database version v2025.09.25. [Internet]. [cited 2025 Sep 26]. Available from: ⟨https://next-gen.materialsproject.org/materials/mp-761059?_sort_fields=density&formula=Na3V2%28PO4%293⟩.
[130] Data retrieved from the Materials Project for Na3V2(PO4)3 (mp-776557) from database version v2025.09.25. [Internet]. [cited 2025 Sep 26]. Available from: ⟨https://next-gen.materialsproject.org/materials/mp-776557?_sort_fields=density&formula=Na3V2%28PO4%293⟩.
[131] Villars P., Cenzual K., editors. Na2V2(PO4)3 (Na3V2[PO4]3 ht3) Crystal Structure: Datasheet from "PAULING FILE Multinaries Edition – 2022" in SpringerMaterials (⟨https://materials.springer.com/isp/crystallographic/docs/sd_1520007⟩) [Internet]. Springer-Verlag Berlin Heidelberg & Material Phases Data System (MPDS), Switzerland & National Institute for Materials Science (NIMS), Japan; [cited 2025 Sep 26]. Available from: ⟨https://materials.springer.com/isp/crystallographic/docs/sd_1520007⟩.
[132] L. Wang, Y.N. Sun, X.D. Wei, M. Yin, Y. Chen, H. Miura, et al., Phys. Chem. Chem. Phys. 25 (48) (2023) 32845–32852, https://doi.org/10.1039/D3CP04563C.
[133] G. Wang, Z.H. Yao, K. Suzuki, Y. Chen, L. Wang, Dalton Trans. 54 (31) (2025) 11914–11924, https://doi.org/10.1039/D5DT01119A.
[134] Villars P., Cenzual K., editors. Na2Fe2(CN)6·2H2O (NaFe[CN]3[H2O]) Crystal Structure: Datasheet from "PAULING FILE Multinaries Edition – 2022" in SpringerMaterials (⟨https://materials.springer.com/isp/crystallographic/docs/sd_1044875⟩) [Internet]. Springer-Verlag Berlin Heidelberg & Material Phases Data System (MPDS), Switzerland & National Institute for Materials Science (NIMS), Japan; [cited 2025 Sep 26]. Available from: ⟨https://materials.springer.com/isp/crystallographic/docs/sd_1044875⟩.
[135] A. Bhattacharjee, S. Saha, S. Koner, Y. Miyazaki, J. Magn. Magn. Mater. 312 (2) (2007) 435–442, https://doi.org/10.1016/j.jmmm.2006.11.188.
[136] Villars P., Cenzual K., editors. Na2Mn[Fe(CN)6]·2H2O (Na1.68MnFe[CN]6[H2O] 2) Crystal Structure: Datasheet from "PAULING FILE Multinaries Edition – 2022" in SpringerMaterials (⟨https://materials.springer.com/isp/crystallographic/docs/sd_1535192⟩) [Internet]. Springer-Verlag Berlin Heidelberg & Material Phases Data System (MPDS), Switzerland & National Institute for Materials Science (NIMS), Japan; [cited 2025 Sep 26]. Available from: ⟨https://materials.springer.com/isp/crystallographic/docs/sd_1535192⟩.
[137] American Elements [Shop] [Internet]. [cited 2025 Sep 26]. Silicon Powder. Available from: ⟨https://americanelements.com/silicon-powder-7440-21-3⟩.
[138] Data retrieved from the Materials Project for TiNb2O7 (mp-758243) from database version v2025.09.25. [Internet]. 2020 [cited 2025 Sep 26]. Available from: ⟨https://next-gen.materialsproject.org/materials/mp-758243?_sort_fields=density&formula=TiNb2O7⟩ doi:10.17188/1291030.
[139] Data retrieved from the Materials Project for TiNb2O7 (mp-1216971) from database version v2025.09.25. [Internet]. [cited 2025 Sep 26]. Available from: ⟨https://next-gen.materialsproject.org/materials/mp-1216971?_sort_fields=density&formula=TiNb2O7⟩.
[140] Villars P., Cenzual K., editors. TiNb2O7 Crystal Structure: Datasheet from "PAULING FILE Multinaries Edition – 2022" in SpringerMaterials (⟨https://materials.springer.com/isp/crystallographic/docs/sd_1401126⟩) [Internet]. Springer-Verlag Berlin Heidelberg & Material Phases Data System (MPDS), Switzerland & National Institute for Materials Science (NIMS), Japan; [cited 2025 Sep 26]. Available from: ⟨https://materials.springer.com/isp/crystallographic/docs/sd_1401126⟩.
[141] Villars P., Cenzual K., editors. TiNb2O7 Crystal Structure: Datasheet from "PAULING FILE Multinaries Edition – 2022" in SpringerMaterials (⟨https://materials.springer.com/isp/crystallographic/docs/sd_1250179⟩) [Internet]. Springer-Verlag Berlin Heidelberg & Material Phases Data System (MPDS), Switzerland & National Institute for Materials Science (NIMS), Japan. Available from: ⟨https://materials.springer.com/isp/crystallographic/docs/sd_1250179⟩.
[142] H. Kim, T.K. Le, M. Kang, J.K. Lee, S.D. Park, S.W. Kim, Mater. Lett. 277 (2020) 128394, https://doi.org/10.1016/j.matlet.2020.128394.
[143] Data retrieved from the Materials Project for LiV2O5 (mp-777667) from database version v2025.09.25. [Internet]. 2020 [cited 2025 Sep 26]. Available from: ⟨https://next-gen.materialsproject.org/materials/mp-777667?_sort_fields=density&formula=LiV2O5⟩ doi:10.17188/1305219.
[144] Data retrieved from the Materials Project for LiV2O5 (mp-19013) from database version v2025.09.25. [Internet]. 2020 [cited 2025 Sep 26]. Available from: ⟨https://next-gen.materialsproject.org/materials/mp-19013?_sort_fields=density&formula=LiV2O5⟩ doi:10.17188/1193800.
[145] American Elements [Shop] [Internet]. [cited 2025 Sep 26]. Vanadium Pentoxide. Available from: ⟨https://americanelements.com/vanadium-pentoxide-1314-62-1⟩.
[146] Villars P., Cenzual K., editors. V2O5 Crystal Structure: Datasheet from "PAULING FILE Multinaries Edition – 2022" in SpringerMaterials (⟨https://materials.springer.com/isp/crystallographic/docs/sd_0452521⟩) [Internet]. Springer-Verlag Berlin Heidelberg & Material Phases Data System (MPDS), Switzerland & National Institute for Materials Science (NIMS), Japan; [cited 2025 Sep 26]. Available from: ⟨https://materials.springer.com/isp/crystallographic/docs/sd_0452521⟩.
[147] Villars P., Cenzual K., editors. δ-LiV2O5 (LiV2O5 rt) Crystal Structure: Datasheet from "PAULING FILE Multinaries Edition – 2022" in SpringerMaterials (⟨https://materials.springer.com/isp/crystallographic/docs/sd_1102469⟩) [Internet]. Springer-Verlag Berlin Heidelberg & Material Phases Data System (MPDS), Switzerland & National Institute for Materials Science (NIMS), Japan; [cited 2025 Sep 26]. Available from: ⟨https://materials.springer.com/isp/crystallographic/docs/sd_1102469⟩.
[148] Villars P., Cenzual K., editors. γ-LiV2O5 (LiV2O5 ht2) Crystal Structure: Datasheet from "PAULING FILE Multinaries Edition – 2022" in SpringerMaterials (⟨https://materials.springer.com/isp/crystallographic/docs/sd_1102470⟩) [Internet]. Springer-Verlag Berlin Heidelberg & Material Phases Data System (MPDS), Switzerland & National Institute for Materials Science (NIMS), Japan; [cited 2025 Sep 26]. Available from: ⟨https://materials.springer.com/isp/crystallographic/docs/sd_1102470⟩.
[149] Villars P., Cenzual K., editors. ϵ-Li0.5V2O5 (LiV2O5 ht1) Crystal Structure: Datasheet from "PAULING FILE Multinaries Edition – 2022" in SpringerMaterials (⟨https://materials.springer.com/isp/crystallographic/docs/sd_1641634⟩) [Internet]. Springer-Verlag Berlin Heidelberg & Material Phases Data System (MPDS), Switzerland & National Institute for Materials Science (NIMS), Japan; [cited 2025 Sep 26]. Available from: ⟨https://materials.springer.com/isp/crystallographic/docs/sd_1641634⟩.
[150] A. Jain, S.P. Ong, G. Hautier, W. Chen, W.D. Richards, S. Dacek, et al., APL Mater. 1 (1) (2013) 12, https://doi.org/10.1063/1.4812323.
[151] J.E. Hurst, K. Harrison, Chem. Eng. Commun. 112 (1) (1991) 21–30, https://doi.org/10.1080/00986449208935989.
[152] M.J. Kriegel, D. Pavlyuchkov, O. Fabrichnaya, M. Rohde, D. Rafaja, H.J. Seifert, J. Phase Equilib. Diffus 35 (6) (2014) 658–665, https://doi.org/10.1007/s11669-014-0332-8.
[153] T. Zienert, O. Fabrichnaya, Calphad 65 (2019) 177–193, https://doi.org/10.1016/j.calphad.2019.01.017.
[154] D. Oehler, J. Bender, P. Seegert, T. Wetzel, Energy Tech. 9 (20200722) (2021) 16, https://doi.org/10.1002/ente.202000722.
[155] P. Zehner, E.U. Schlünder, Chem. Ing. Tech. 42 (14) (1970) 933–941, https://doi.org/10.1002/cite.330421408.
[156] P. Zehner, E.U. Schlünder, Chem. Ing. Tech. 44 (23) (1972) 1303–1308, https://doi.org/10.1002/cite.330442305.

[157] P. Zehner, E.U. Schlünder, Chem. Ing. Tech. 45 (5) (1973) 272–276, https://doi.org/10.1002/cite.330450509.
[158] R.L. Hamilton, O.K. Crosser, Ind. Eng. Chem. Fund. 1 (3) (1962) 187–191, https://doi.org/10.1021/i160003a005.
[159] P. Seegert, Simulative Untersuchung des multiphysikalischen Verhaltens von Lithium-Ionen Zellen [Dissertation] [Internet], Karlsruher Institut für Technologie, Karlsruhe, 2021, https://doi.org/10.5445/IR/1000143482.
[160] E.G. Gilbert, D.W. Johnson, S.S. Keerthi, IEEE J. Robot Autom. 4 (2) (1988) 193–203, https://doi.org/10.1109/56.2083.
[161] L. Pfaffmann, S. Jaiser, M. Müller, P. Scharfer, W. Schabel, W. Bauer, et al., J. Power Sources 363 (2017) 460–469, https://doi.org/10.1016/j.jpowsour.2017.07.102.
[162] B.F. Baggio, C. Vicente, S. Pelegrini, C.C. Plá Cid, I.S. Brandt, M.A. Tumelero, et al., Materials 12 (1103) (2019) 9, https://doi.org/10.3390/ma12071103.
[163] IEEE Comput Grap Appl. 1981;1(1):11–23. doi:10.1109/MCG.1981.1673799.
[164] Becker V.I. Modellierung der Mechanik und der effektiven Transporteigenschaften von partikulären Kathoden sowie deren Einfluss auf die elektrochemische Performance von Lithium-Ionen-Batterien [Dissertation] [Internet]. [Karlsruhe]: Karlsruher Institut für Technologie; 2021 [cited 2026 Feb 18]. Available from: ⟨https://publikationen.bibliothek.kit.edu/1000143718⟩ doi:10.5445/KSP/1000143718.
[165] J. Asenbauer, T. Eisenmann, M. Kuenzel, A. Kazzazi, Z. Chen, D. Bresser, Sustain Energy Fuels 4 (2020) 5387–5416, https://doi.org/10.1039/D0SE00175A.
[166] N.E.I. Corporation. Material Characterisitcs CBP-58 [Specification Sheet] [Internet]. 2024 [cited 2024 Nov 4]. Available from: ⟨https://www.neicorporation.com/products/batteries/cathode-anode-powders/lithium-ion/⟩.
[167] N.E.I. Corporation. Active Material Characterisitcs ABP-200 [Specification Sheet] [Internet]. 2024 [cited 2026 Jan 18]. Available from: ⟨https://www.neicorporation.com/products/batteries/cathode-anode-powders/lithium-ion/⟩.
[168] N.E.I. Corporation. Material Characteristics Nanomyte NAB-80 (Prussian Blue) [Specification Sheet] [Internet]. 2023 [cited 2024 Nov 5]. Available from: ⟨https://www.neicorporation.com/products/batteries/cathode-anode-powders/sodium-ion/⟩.
[169] M. Steinhardt, E.I. Gillich, M. Stiegler, A. Jossen, J. Energy Storage 32 (101680) (2020) 12, https://doi.org/10.1016/j.est.2020.101680.